European Commission

JRC TECHNICAL REPORTS

Analysis of Adjacency Effects for Copernicus Ocean Colour Missions

Barbara Bulgarelli and Giuseppe Zibordi

2018

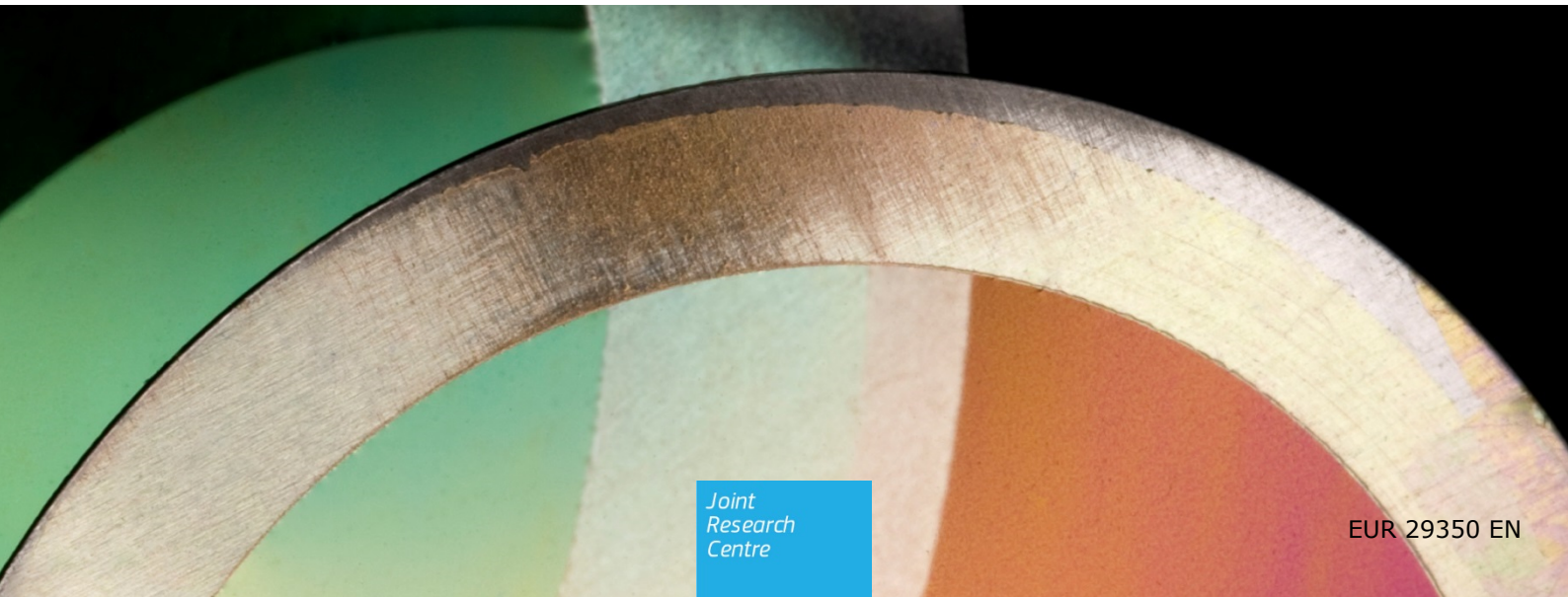

Joint Research Centre

EUR 29350 EN

This publication is a Technical report by the Joint Research Centre (JRC), the European Commission's science and knowledge service. It aims to provide evidence-based scientific support to the European policymaking process. The scientific output expressed does not imply a policy position of the European Commission. Neither the European Commission nor any person acting on behalf of the Commission is responsible for the use that might be made of this publication.

Contact information
Name: Barbara Bulgarelli
Address: JRC-EC, 21020 Ispra (I)
Email: barbara.bulgarelli@ec.europa.eu
Tel.: 0039-0332-785778

EU Science Hub
https://ec.europa.eu/jrc

JRC112829

EUR 29350 EN

PDF	ISBN 978-92-79-96686-6	ISSN 1831-9424	doi:10.2760/178467
Print	ISBN 978-92-79-96687-3	ISSN 1018-5593	doi:10.2760/851541

Luxembourg: Publications Office of the European Union, 2018

How to cite this report: Barbara Bulgarelli and Giuseppe Zibordi, *Analysis of Adjacency Effects for Copernicus Ocean Colour Missions*, EUR 23950 EN, 2018, Publications Office of the European Union, Luxemburg, ISBN 978-92-79-96686-6, doi:10.2760/178467, JRC112829.

This is a re-edition of: Barbara Bulgarelli and Giuseppe Zibordi, *Analysis of Adjacency Effects for Copernicus Ocean Colour Missions*, EUR 23950 EN, 2018, Publications Office of the European Union, Luxemburg, ISBN 978-92-79-93671-5, doi:10.2760/43628, JRC112829.

Contents

Forward

The Copernicus Programme was established by the European Union (Regulation EU No377/2014) to develop European information services based on satellite Earth Observation (EO) and *in situ* data.

Among the six Copernicus Services, the Copernicus Marine Environment Monitoring Service (CMEMS) and the marine component of the Copernicus Climate Change Service (C3S) both rely on EO data delivered by satellite ocean color (OC) sensors, i.e., primary OC radiometric products (such as the radiance L_w leaving the water body) and Chlorophyll-a concentrations (Chl_a, a proxy for phytoplankton biomass). These variables, able to provide unique monitoring capabilities of the green marine environment, have been identified by the Global Ocean Observing System (GOOS) as Essential Ocean Variables (EOV) to monitor the health of the oceans, and by the Global Climate Observation System (GCOS) as Essential Climate Variable (ECV) to support the work of the United Nations Framework Convention on Climate Change (UNFCCC).

ECV contributing to the creation of Climate Data Records (CDRs) needs to accomplish high accuracy requirements.

This is particularly demanding in coastal water, where the simultaneous presence of non-covarying in-water optically active components (i.e., pigments, colored dissolved organic matter and suspended sediments) and potential contributions from sea-bottom and nearby land leads to rather complex bio-optical properties. As such, while the determination of the optical properties of the open ocean from satellite measurements is nowadays largely established, the remote sensing of coastal waters still represents an open challenge.

Nonetheless, the economical and environmental importance of coastal zones is widely acknowledged: a large portion of the global population lives in coastal areas, whereas coastal marine habitats are extremely sensitive to the impacts of climate variability and change. A specific action for the coordination of enhanced shelf and coastal observations for climate has been indeed designed by the GCOS Implementation Plan (GCOS, 2016) with the aim to define detailed specific observational requirements for an improved understanding, assessment and prediction of the impact of climate in the coastal environment.

ECV high accuracy requirements imply a thorough evaluation of the uncertainties affecting satellite and *in situ* data, and the procedures applied for the retrieval of OC products from the satellite observations.

The present report focuses on the uncertainties induced by nearby land in OC observations of coastal regions, summarizing most recent quantifications and analyses.

The content of the Report builds on the long-standing experience of the JRC on the modeling of OC satellite and *in situ* observations.

Acknowledgements

The content of this Report summarizes results published in peer review literature by the same authors in collaboration with a number of colleagues whose contribution is duly acknowledged. Specifically, grateful thanks are due to: Dr. Frederic Mèlin from the JRC and Dr. Viatchelsav Kiselev, from EOMAP GmbH and Co.

This Report is a contribution to *Earth Observation Support to Copernicus Climate and Marine Services* (EOSS) funded by the Joint Research Centre (JRC).

Authors

Barbara Bulgarelli, EC-JRC, Ispra (VA) - I

Giuseppe Zibordi, EC-JRC, Ispra (VA) - I

Abstract

The present report focuses on the uncertainties induced by nearby land in OC observations of coastal regions, summarizing most recent quantifications and analyses. Standard algorithms for the processing of satellite data generally assume an infinite water surface, and hence neglect the presence of the nearby land. As a consequence, the radiance reflected by the land and then scattered by the atmosphere in the field of view of a satellite sensor observing a water target represents a source of perturbations leading to uncertainties in OC products. This phenomenon is called *adjacency effects* (AE), and always occurs in the presence of a scattering medium overlaying a surface of non-homogeneous reflecting properties.

Specific attention is given to AE affecting marine observations by two EO-dedicated satellite sensors of the Copernicus Space component: i) the Ocean and Land Colour Instrument (OLCI) on board Sentinel-3, specifically developed to deliver OC observations of the sea; and ii) the MultiSpectral Imagery (MSI) on board Sentinel-2, which, aims at providing high-resolution optical land imagery, but also acquires data up to 20 km offshore.

AE are quantified and analyzed for a wide range of typical mid-latitude coastal environments and for specific case studies, i.e., the Aqua Alta Oceanographic Tower (AAOT) validation site located in the Northern Adriatic Sea, included in the Ocean Color component of the Aerosol Robotic Network (AERONET-OC), also considered for vicarious calibrations of marine MSI data; and the marine region surrounding the Lampedusa Island located in the Southern Mediterranean Sea, hosting a validation site, and considered for long-term vicarious calibrations of OLCI data.

The study analyzes the relevance of AE in the signal at the sensor with regard to standardized signal-to-noise ratios (SNR). Considerations are also drawn on perturbations induced by AE in satellite radiometric products.

The content of this Report builds on the long-standing experience of the JRC on the modeling of OC satellite and *in situ* observations. This experience counts on the development and decadal utilization of highly accurate radiative transfer models (RTM) for the propagation of the solar radiation in the atmosphere-ocean system. These in-house modeling capabilities (the Advanced Radiative Transfer Models for In-situ and Satellite Ocean color data, ARTEMIS-OC) comprise a plane-parallel numerical RTM based on the finite element method and a three-dimensional (3D) MonteCarlo (MC) code.

Overall, this Report summarizes a number of recent investigations led by the JRC on AE in satellite observations of coastal waters. The final objective is to consolidate in a single document theoretical findings and considerations about adjacency perturbations from nearby land in the coastal remote sensing observations performed within the Copernicus Programme.

Briefly, the various Chapters summarize:

- *The general definition and description of the AE, while briefly illustrating the applied modeling technique;*
- *The theoretical quantification of AE for a wide range of typical mid-latitude coastal environments.*
- *The theoretical evaluation of AE at the AAOT and Lampedusa validation sites.*

1. Introduction

> *"The more we learn about the world, and the deeper our learning, the more conscious, specific, and articulate will be our knowledge of what we do not know, our knowledge of our ignorance" - Karl Popper*

Primary OC data products, like the spectral water-leaving radiance L_W or alternatively the derived remote sensing reflectance R_{RS}, quantify the light emerging from the sea and are applied to determine geophysical quantities such as the near-surface chlorophyll-a concentration Chl_a. The accuracy of primary radiometric products (required by GCOS to not exceed 5% with respect to oceanic waters in the blue-green spectral bands) hence determines the accuracy of such derived quantities (for Chl_a GCOS requires a maximum uncertainty of 30%).

The water-leaving radiance L_W is in turn determined from the top of the atmosphere radiance L_{tot} through a correction scheme apt to remove those radiance contributions that do not arise from the interaction of the sunlight with the water. Since L_w is only a few percent of L_{tot}, it is clear that uncertainties in the processing scheme may induce significant perturbations in L_w, thus limiting the capability to meet the GCOS accuracy requirements.

Uncertainties in the processing scheme can be efficiently investigated through accurate RTMs, able to theoretically reconstruct the different components of the signal at the sensor by accounting for any possible interaction of the solar radiation with the optically active components of the system. Modeling capabilities are thus central to the evaluations of ECVs uncertainty.

Accurate and efficient modeling capabilities in turn rely on i) accurate radiative transfer algorithms, mathematically describing in a correct and coherent way the propagation of the radiance through a defined system, and ii) an accurate optical characterization of the medium in which the radiance propagates. It is clear that the latter highly benefits from extensive and accurate *in situ* measurements of the inherent (IOPs) and apparent (AOPs) optical properties of the system. It is conclusively the synergetic use of robust and efficient radiative transfer algorithms and accurate *in situ* measurements, which allows the greatest modeling capabilities.

The robust, efficient and accurate in-house modeling capabilities of ARTEMIS-OC thus benefits of the long-lasting experience of the JRC in RTMs and *in situ* observations.

The modeling approach has been here applied to estimate AE induced by land in coastal waters. The *adjacency radiance* L_{adj}, used to quantify the AE, is a contribution to the signal at the sensor commonly neglected by standard processing schemes of OC satellite data, which thus introduces uncertainties in current data products.

The present Report summarizes key findings on AE with respect to the radiometric sensitivity of the OC sensors. The overall aim is an evaluation of biases induced by AE in processing schemes deriving L_w from remote observations of coastal areas, and a better determination of uncertainties affecting validation and calibration analysis at sites. Specific reference is given to mid-latitude seas and to the Copernicus OC missions.

Focus is placed into *i.* The theoretical estimate of AE in Copernicus OC data from coastal regions, *ii.* The analysis of AE with respect to the spectral resolution of the satellite radiometers, and *iii*. Recommendations for the calibration and processing of

Copernicus OC data from coastal regions, as well as for the planning of future missions focused on the exploitation of data acquired in coastal areas.

2. Theoretical estimate of AE in OC data from coastal regions

2.1 The Adjacency Effects

The atmosphere diffuses in all directions the radiance reflected by the underlying surface. As a consequence, radiance from high-reflectivity areas spills over neighboring low-reflectivity regions, so that the apparent brightness of the surface is modified (Otterman and Fraser, 1979).

Such a phenomenon is called *adjacency effects*, and its quantification is made in terms of the *adjacency radiance* L_{adj}, defined as the difference in the radiance at the sensor between the case accounting for the non-uniformity of the underlying reflecting surface and the case assuming a uniform surface. As such, L_{adj} can range from negative to positive values.

The problem of AE in land satellite observations has been extensively investigated for decades (see Tanre et al., 1979; Kaufman, 1979; Kaufman, 1984; Pearce, 1986, and references therein), and has led to the implementation of atmospheric correction codes correcting for adjacency perturbations. Examples are the NASA MOD09 atmospheric correction algorithm (Vermote and Vermeulen, 1999), and commercial atmospheric correction software packages such as the Fast Line-of-sight Atmospheric Analysis of Hypercubes (FLAASH) (Adler-Golden et al., 1999), and the Atmospheric and Topographic Correction (ATCOR) (Richter and Schlapfer, 2018). Notably, operational Landsat-based processing for large-scale product generation do not currently correct for AE (Houborg and McCabe, 2017; Masek et al., 2006)

Conversely, fewer past studies specifically addressed AE in coastal waters (Reinersman and Carder, 1995; Yang et al., 1995; Santer and Schmechtig, 2000; Ruddick et al., 2000; Sei, 2007; Sei, 2015; Bélanger et al., 2007), and most of them applied one or more simplifying assumptions [e.g., nadir observation (Sei, 2007), straight coastline (Sei, 2007), Lambertian reflecting land and sea (Reinersman and Carder, 1995; Sei, 2007), single scattering (Santer and Schmechtig, 2000), and exponential decay of the background effects (Santer and Schmechtig, 2000; Sei, 2007)]. Additionally, uncertainties on simulated results were never explicitly discussed, and the radiometric sensitivity of the measuring sensors, which implicitly defines the threshold for discriminating AE from noise, was never taken into consideration.

On top of this, standard processing techniques of OC data generally assume an infinite water surface (Antoine and Morel, 1999; Gordon and Wang, 1994) altogether neglecting AE even in the proximity of land. Mention is given to the few available processors for the correction of AE in coastal and inland waters: the adjacency correction algorithm by Kiselev et al., (2015) included in the Modular Inversion Program (Heege, Kiselev, Wettle, and Hung, 2014); the SIMilarity Environment Correction (SIMEC) (Sterckx et al., 2015) integrated in the atmospheric image CORrection for land and water (iCOR) (Sterckx, 2017); the Improve Contrast between Ocean and Land (ICOL) used to correct MERIS images (Santer and Zagolski, 2009); and the algorithm proposed by (Sei, 2015).

It is clear that neglected adjacency contributions become source of spectral perturbations in satellite data, leading to uncertainties in derived primary products.

Within the framework of the continuous multi-annual effort put by the JRC to identify, quantify and minimize uncertainties affecting OC primary products (Bulgarelli and Zibordi, 2003; Mélin et al., 2016; Zibordi et al., 2009a), and amply justified by the lack of exhaustive scientific knowledge of AE in satellite acquisitions from coastal waters, an extensive and comprehensive theoretical analysis of AE has

been performed (Bulgarelli et al., 2014; 2017; 2018c; Bulgarelli and Zibordi, 2018a; 2018b)

2.2 The simulation procedure

The adjacency radiance L_{adj} and its percent contribution to L_{tot} have been simulated making use of the RTMs included in the ARTEMIS-OC software package, namely the numerical code based on the Finite Element method for the simulation of OC satellite data (FEMRAD-OC) (Bulgarelli et al., 1999) and the Novel Adjacency Perturbation Simulator for Coastal Areas (NAUSICAA) full three-dimensional (3D) backward MC code (Bulgarelli et al., 2014).

The plane-parallel FEMRAD-OC code is used to simulate radiance contributions at the sensor, which can be reasonably assumed as horizontally invariant, e.g., the atmospheric radiance and its components. The 3D NAUSICAA code is instead used to simulate the adjacency radiance. All simulations are performed for a stratified atmosphere (modeling the vertical distribution of gas molecules and aerosol) bounded by a Fresnel reflecting surface, fully accounting for multiple scattering, sea surface roughness, slanted illumination and observation conditions. NAUSICAA simulations additionally include a non-uniform reflecting surface, with detailed description of the coastal morphology.

In order to reduce computing time for the MC simulations, the adjacency radiance has been modeled as:

$$L_{adj}=\{\rho_l \cdot \kappa_l - R_{rs} \cdot \kappa_w\} \cdot C^{\rho=1} - W \ , \qquad (1)$$

where the albedo of the land ρ_l and the remote sensing reflectance R_{RS} have been both assumed isotropic and spatially homogeneous; the functions $C^{\rho=1}$ and W designate the cumulative radiance contribution at the sensor originating from the land assumed as an ideal Lambertian reflector (Martonchik et al., 2000) and as a Fresnel wind-roughened sea surface, respectively; and parameters κ_l and κ_w are scaling factors to adjust the radiance reflected by an ideal Lambertian reflector to that reflected by an actual land surface and to that leaving the water volume, respectively (see Bulgarelli et al., 2014 and 2018c for more details). The term W is often called the *Fresnel mask* (Santer and Schmechtig, 2000).

The proposed modeling allows to decouple land and water optical properties from the atmospheric scattering, while accurately describing the anisotropy of the sea surface (modeled according to Kisselev and Bulgarelli, 2004). Once the functions $C^{\rho=1}$ and W are computed for given geometric and atmospheric inputs, Eq. (1) allows a straightforward evaluation of the AE for a wide variety of land and water spectral signatures. The latter can be extrapolated from satellite-derived or *in situ* measured data.

Statistical uncertainties on MC computations were required not to exceed the average resolution of the Sea Wide Field of View Sensor (SeaWiFS), the Moderate Resolution Imaging Spectroradiometer (MODIS) and the Medium Resolution Imaging Spectrometer (MERIS) OC sensors (Bulgarelli et al., 2014). Systematic uncertainties were evaluated to be always lower than the statistical uncertainty of NAUSICAA simulations with a 99.7% level of confidence (Bulgarelli et al., 2014).

3. Harmonized sensor radiometric sensitivity

A cross-analysis of AE among different sensors requires the SNR to be defined and computed in a harmonized way, i.e., for the same input signal.

In modern radiometers, detector and readout noise are dominated by the shot (or photon) noise, which describes the variation in the number of photons detected by the sensor per unit time, and whose standard deviation is the square root of the input radiance (Moses et al., 2012). This property has been utilized to scale latest on-orbit performance SNR of OLCI and MSI (specified for given reference input radiances L_{ref}) to the input radiance L_{typ} typical of cloud-free ocean scenes (see Table 1 and 2, respectively). Notably, since L_{ref} for MSI is more than 50% larger than L_{typ}, the scaled SNR for MSI might underestimate the actual values by more than 10% (Hu et al., 2012).

Harmonized values of the noise level NL=100/SNR (to which the percent contribution of AE at the sensor is compared) are spectrally represented in Fig. 1 at SeaWiFS-equivalent center-wavelengths (highlighted in Table 1 and 2). OLCI band at 778 nm has been selected among other several bands close to 765 nm being utilized to perform the atmospheric corrections (Antoine and Morel, 1999). Notably, OLCI acquires data in full (0.3 km, FR) and reduced (1.2 km, RR) spatial resolution with significantly different SNR. For comparison, NL for SeaWiFS, MODIS-Aqua, MERIS-RR, MERIS-FR and the Landsat-8 Operational Land Imager (OLI), measured at or adjusted to the same input radiance L_{typ}, are also illustrated (Bulgarelli and Zibordi, 2018a).

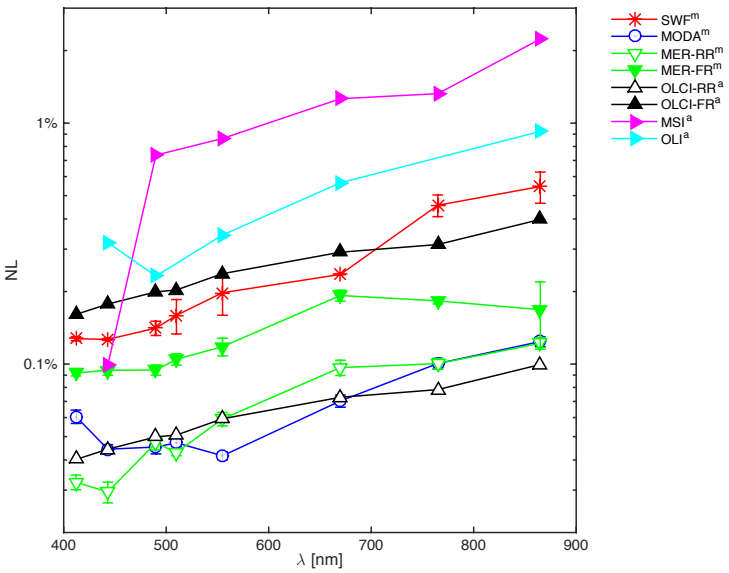

Figure 1. Spectral values of NL=1/SNR (in percent) at SeaWiFS-equivalent wavelengths for selected sensors. Suffix 'm' indicates that SNRs were measured on-orbit (Hu et al., 2012). Suffix 'a' indicates that SNRs were adjusted to L_{typ} (Bulgarelli and Zibordi, 2018a)

Highest radiometric sensitivity characterizes MODIS-Aqua, MERIS-RR and OLCI-RR data. In specific, MERIS-RR is the most sensitive sensor at the blue-green wavelengths, MODIS-Aqua around 555 nm, OLCI-RR at longer wavelengths. The radiometric sensitivity of MERIS-FR is slightly larger than that of SeaWiFS, while the radiometric performance of OLCI-FR (¼ of that of OLCI-RR) is slightly lower. As expected, the largest NL values are found for the MSI and OLI sensors, which were developed for land applications. Indeed, land observations require a high geometric

resolution to capture the large spatial variability of land optical properties, and a high radiometric range to accommodate signals from bright targets, while they do not need the high radiometric resolution required by OC sensors to discriminate the small variations of the water signal. Notably, the NL of the MSI band at 443 nm (characterized by the coarsest MSI spatial resolution) is significantly lower, and close to that of MERIS-FR. At other bands the NL of MSI becomes instead the highest. It is mentioned that MODIS land bands (with 250-500 m spatial resolution), also used for OC applications, are characterized by NL values lying in between those of OLI and MSI.

Table 1. OLCI-RR tabulated spectral values of SNR@L_{typ} of latest on-orbit performance SNR after adjustment to the typical input radiance $\mathbf{L_{typ}}(\boldsymbol{\theta_0} = \mathbf{45^o})$ given in (Hu et al., 2012). The SNR values at reference input radiance L_{ref} [$Wm^{-2}\mu m^{-1}sr^{-1}$] from specifications (SNR@L_{ref}) are also indicated. OLCI-RR measurements are performed with spatial resolution Δs=1200 m at all bands. The radiometric performance of OLCI-FR acquisitions (Δs=300 m) is ¼ of that of OLCI-RR. Center-wavelengths λ and bandwidths Δλ are in nm. The SeaWiFS-equivalent center-wavelengths utilized in the study are indicated in bold. [[1]from S3 MPC (02/2017)]

λ	***Δλ***	***SNR@L_{typ}***	***SNR@L_{ref}*** [1]	***L_{ref}***
400	15	2736.4	2356	62.95
412.5	**10**	**2488.7**	**2388**	**74.14**
442.5	**10**	**2254.5**	**2183**	**65.61**
490	**10**	**2006.0**	**2000**	**51.21**
510	**10**	**1969.6**	**1985**	**44.39**
560	**10**	**1686.0**	**1798**	**31.49**
620	10	1481.0	1607	21.14
665	**10**	**1373.3**	**1553**	**16.38**
673.75	7.5	1179.0	1337	15.70
681.25	7.5	1166.6	1326	15.11
708.75	10	1260.0	1424	12.73
753.75	7.5	959.5	1128	10.33
761.25	2.5	541.4	502	6.09
764.375	3.75	656.2	663	7.13
767.5	2.5	532.8	559	7.58
778.75	**15**	**1276.1**	**1513**	**9.18**
865	**20**	**1004.2**	**1238**	**6.17**
885	10	665.4	819	6.00
900	10	619.0	688	4.73
940	20	643.2	533	2.39
1020	40	293.7	346	3.86

Table 2. MSI tabulated spectral values of SNR@L_{typ} (see Table 2) The spatial resolution Δs [m] is also indicated. [[1]from S2 MPC]

λ	***Δλ***	***Δs***	***SNR@L$_{typ}$***	***SNR@L$_{ref}$*** [1]	***L$_{ref}$***
443	**20**	**60**	**1009.2**	**1372**	**129**
490	**65**	**10**	**135.8**	**214**	**128**
560	**35**	**10**	**115.8**	**249**	**128**
665	**30**	**10**	**79.2**	**230**	**108**
705	15	20	93.6	253	74.5
740	**15**	**20**	**75.5**	**220**	**68**
783	20	20	70.1	227	67
842	115	10	46.4	221	103
865	**20**	**20**	**44.8**	**161**	**52.5**
945	20	60	137.2	222	9
1375	30	60	130.8	390	6
1610	90	20	47.1	159	4
2190	180	20	40.3	217	1.5

4. Relevance of adjacency perturbations with respect to the radiometric resolution of satellite sensors

In the following the relevance of AE with respect to the radiometric resolution of OLCI and MSI sensors is analyzed by comparing the percentage adjacency contribution at the sensor $\xi_{L_{tot}} = 100 \cdot L_{adj}/L_{tot}$ with the percentage noise level NL=100/SNR. Any adjacency radiance contribution lower than NL is regarded as not discriminable from noise, i.e., not detectable.

Section 4.1 illustrates results for a set of idealized test cases well representing typical mid-latitude coastal environments, while Section 4.2 and 4.3 detail results for two specific test sites: the AAOT validation site (45.31° N, 12.51° E) and the whole marine region surrounding the Lampedusa Island (35.52° N, 12.57° E), respectively. In both latter cases coastal morphology and seasonality of land, water and atmosphere optical properties were thoroughly accounted for.

4.1 Results for typical mid-latitude coastal environments

Theoretical estimates of AE for common mid-latitude coastal environments have been conducted along a study transect extending perpendicular to a half-plane of uniform and isotropic land albedo, whose coastline is oriented in the South-North direction (Fig. 2). The optical properties of the water were assumed to be constant along the study transect.

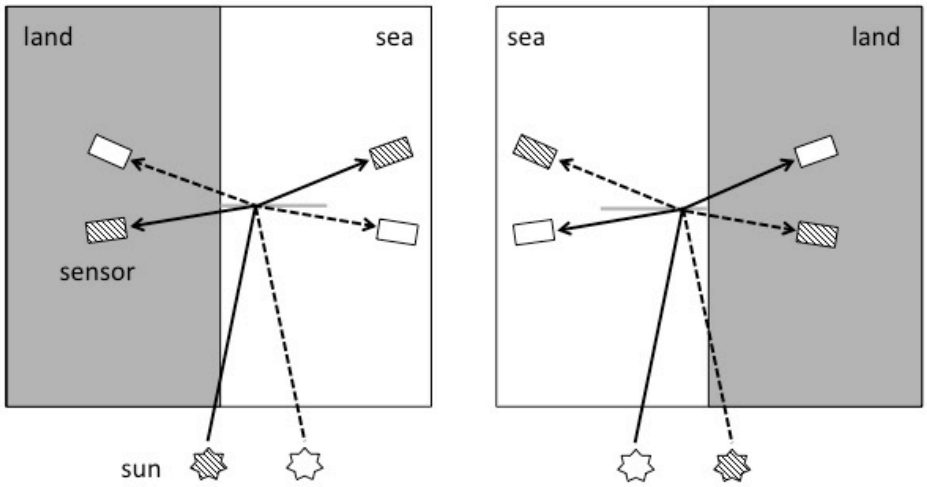

Figure 2. Geometry of illumination and observation adopted in the simulations of Section 4.1. The gray horizontal line represents the study-transect.

Simulations have been performed accounting for:

- *Typical illumination and observation geometries (see Table 3 and Fig. 2).*

- *Typical atmospheric conditions, identified by Ångström exponent v=1.7, Ångström coefficient α=0.05, and wind speed w=3.3 ms^{-1}.*

Table 3. Parameters defining the illumination and observation geometries adopted in the simulations detailed in Sections 4.1, 4.2 and 4.3. θ-angles are determined with respect to the local vertical; ϕ-angles are counted clock-wise from the North direction (as generally adopted in satellite geolocation).

Parameters	***Selected values***
θ_0	45°
θ_v	$5^{o[OLCI,MSI]}$, $20^{o[OLCI,MSI]}$, $50^{o[OLCI]}$
ϕ_0	+160°
ϕ_v	-75° +100°

- *Land cover reflectance spectra found in most frequent terrestrial environments. Spectral directional-hemispherical reflectances (DHR, i.e., the reflectance for incoming light from a single direction (Martonchik et al., 2000)) for grass, dry grass, deciduous trees, conifers, concrete, snow of different grain size, white and brown sand, brown and pale brown loam, were extracted from the Advanced Spaceborne Thermal Emission and Reflection Radiometer (ASTER) spectral library (Baldridge et al., 2009) and were assumed to approximate the land albedo ρ_l (Fig. 3). Although the selection of land covers is not exhaustive, their combination can be considered representative of the ecosystems listed in the IGBP Land Ecosystem Classification Map Image (IGBP Land Ecosystem Classification Map Image, 2013; Malenovský et al., 2012). An actual surface is clearly a composite of different land covers. For example, the cropland ecosystem (covering the land nearby the AAOT, see Section 4.2) can be modeled as a weighted composite of vegetation and soil, which varies according to cropland type, moisture content and phenological state, and whose reflectance is closer to that of vegetation in summer and to that of soil in winter.*

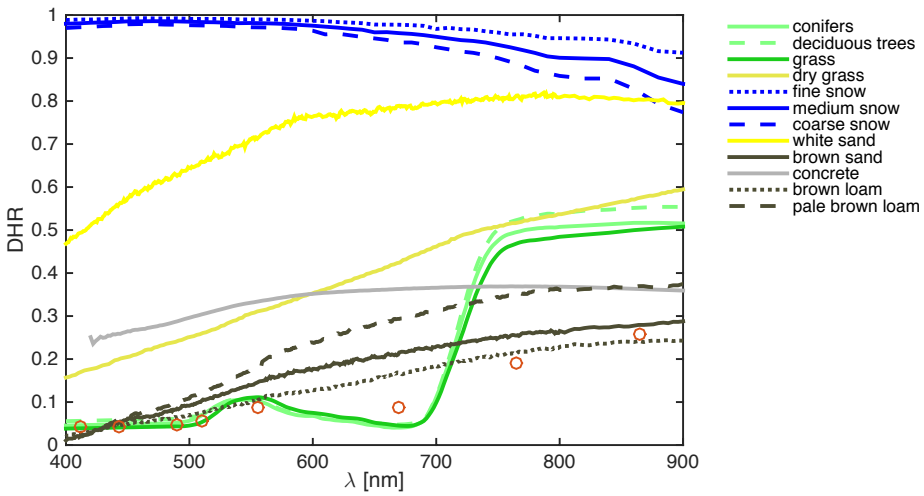

Figure 3. Values of DHR for selected land covers. Empty dots represent the land albedo utilized to simulate AE at the AAOT (see Section 4.2) (Bulgarelli et al., 2014).

- *Spectra of normalized water-leaving radiance characterizing most common European waters (Fig. 4) as taken from the Bio-Optical mapping of Marine*

Properties (BiOMaP) dataset (Zibordi et al., 2011). The sample marine regions embrace a wide set of bio-optical conditions ranging from Case-1 to a number of complex Case-2 waters (Berthon et al., 2008a and references therein). In specific, they include oligotrophic Eastern Mediterranean (EMED) waters; mesotrophic Ligurian Sea (LIGS) waters; northern Adriatic Sea (NADR) and English Channel (ECHN) Case-2 waters, moderately dominated by detritus or mineral particles from rivers discharge or tidal resuspension; Black Sea (BLKS) waters occasionally offering unique concentrations of coccolithophores in the central-western basins and of sediments in proximity of the Danube sea; Baltic Sea (BLTS) Case-2 waters, which are dominated by color dissolved organic matter (CDOM), and which show a high concentration of dissolved humic matter and varying concentration of detritus particles in its different sub-basins (Berthon and Zibordi, 2010). Summary of average IOPs for the selected BiOMaP regions can be found in (Zibordi et al., 2011).

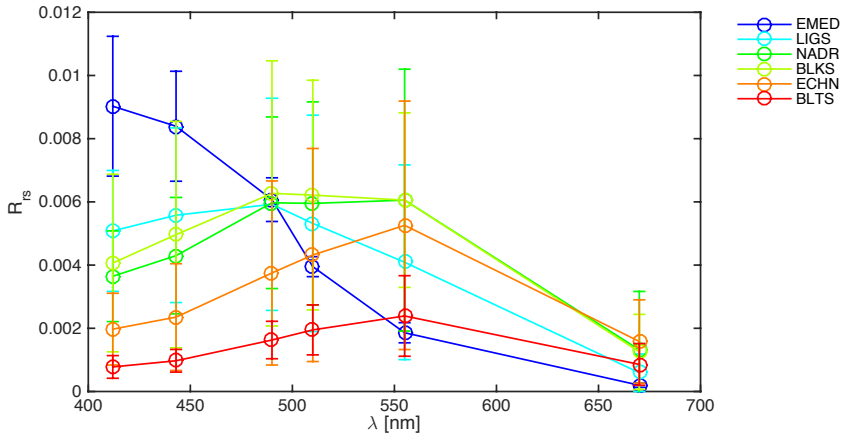

Figure 4. Spectral values of $\bar{\mathbf{R}}_{\mathbf{rs}}$ [sr^{-1}] for selected waters. Error bars indicate standard deviations.

The absolute value of mean adjacency contributions $\bar{\xi}_{L_{tot}}$ (over all observation geometries illustrated in Fig. 2 and Table 3) for NADR waters in the presence of representative land covers are summarized in Fig. 5 at sample center-wavelengths along the study transect, together with sensors NL. Data for fine and coarse snow are neither presented nor discussed since equivalent to those of medium grain snow. Data for conifers and grass, brown sand and pale brown loam have been omitted, being similar to those of deciduous trees and brown loam, respectively.

As expected, values of $|\bar{\xi}_{L_{tot}}|$ monotonically decrease with the distance from the coast, and their magnitude increases with the spectral albedo of the land cover. For both sensors, mean adjacency contributions in the presence of snow, white sand, concrete and dry vegetation are above NL throughout the considered transect and at all wavelengths. Conversely, adjacency contributions in the presence of green vegetation and bare soil might become lower than sensor NL within the transect, at a distance that increases with the radiometric sensitivity of the sensor. It is hence the longest for OLCI-RR, and the shortest for MSI (apart for λ=443 nm, where largest NL occur for OLCI-FR). As an example, perturbations for green vegetation and brown loam at 555 nm become lower than NL at ~3 km offshore for MSI, ~15 km for OLCI-FR, while they are above the noise thresholds throughout the whole 36 km-transect for OLCI-RR. It is noted that for highly sensitive OLCI-RR acquisitions mean adjacency contributions drop below NL at distance from the coast shorter than 36 km at sole red center-wavelengths with green vegetation. It is also

mentioned that green vegetation and bare soil contributions at blue center-wavelengths are negative.

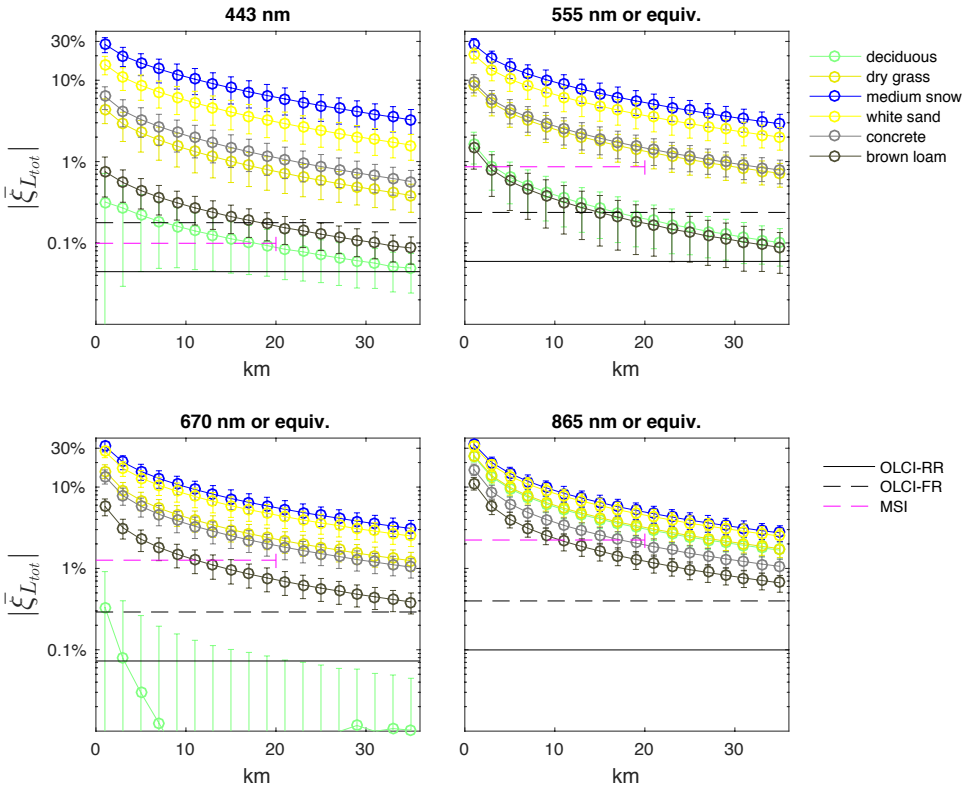

Figure 5. Values of $|\bar{\xi}_{L_{tot}}|$ at representative wavelengths along the study transect as a function of the distance from the coast for NADR Case-2 moderately sediment-dominated waters and different land covers. Error bars represent the standard deviation. Horizontal lines indicate sensors' NL.

Different observation geometries, as well as the mutual location of sun, sensor and land, influence actual adjacency contributions (see Bulgarelli et al., 2014 and 2018c for details). In specific, results highlight a general increase of AE with the viewing angle, as illustrated in Fig. 6 for green grass and snow at 443 and 865 nm. Adjacency perturbations also show a dependence on the position of the sun with respect to the land (Fig. 7), which is more significant when land and sea albedos are closer (as for green vegetation and bare soil at the blue wavelengths). Conversely, when the land reflectance is consistently larger than the sea one (i.e., throughout the spectrum for snow, dry vegetation, white sand and concrete, or at the sole NIR wavelengths for green vegetation and bare soil), AE become sensitive to the position of the sensor with respect to the land (see Fig. 8). This is mainly relevant for slanted observations, for which AE appear consistently larger when the sensor is observing from over the land.

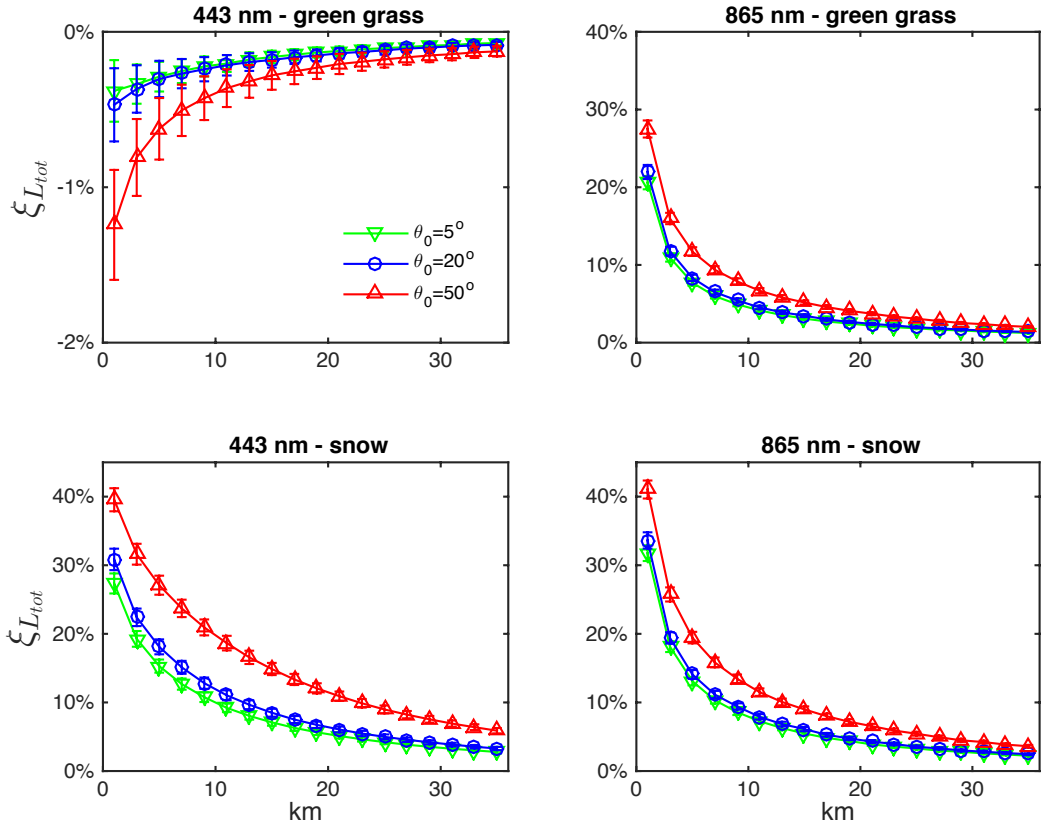

Figure 6. Values of $\xi_{L_{tot}}$ at representative center-wavelengths along the study transect as a function of the distance from the coast for NADR waters in the presence of (upper panels) green grass and (lower panels) snow. Observations are for ϕ_0=160°, ϕ_v= −75° when the land is located in the western half-plane. Error bars represent the standard deviation.

Results from Fig. 6, 7 and 8 allow concluding that actual adjacency contributions are expected to be below the average (illustrated in Fig. 5) for quasi-nadir observations and when the sensor is located over the sea. Conversely, they are expected to be above the average for slanted observations and when the sensor is located over the land. It is remarked that adjacency perturbations are expected to be more dependent on the sun-sensor position for a coast oriented in the East-West direction.

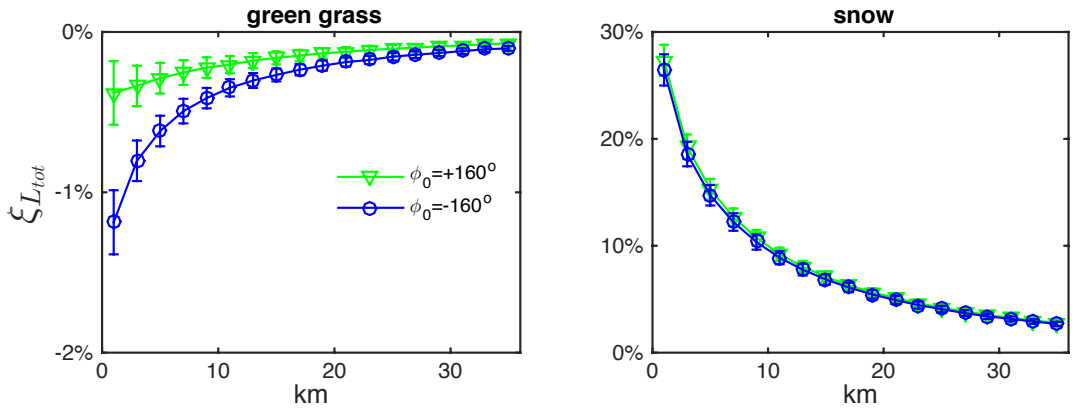

Figure 7. Values of $\xi_{L_{tot}}$ at 443 nm along the study transect as a function of the distance from the coast for NADR waters in the presence of (left panels) green grass and (right panels) snow. Observations are from over the land (located in the western half-plane) and for θ_v=5°. Error bars represent the standard deviation.

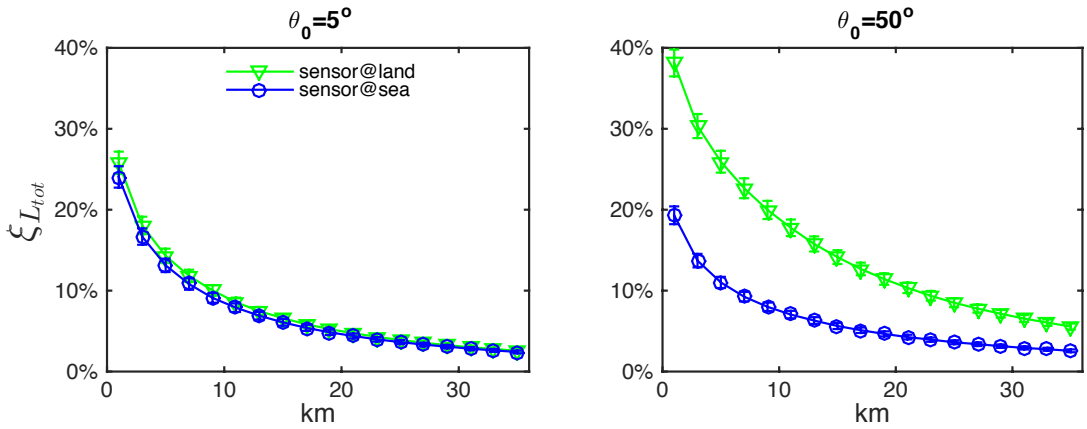

Figure 8. Values of $\xi_{L_{tot}}$ at 443 nm along the study transect as a function of the distance from the coast for NADR waters in the presence of snow. Observations are for ϕ_0=160° and land located in the western half-plane, while the satellite viewing angle is θ_v=5° (left panel) and θ_v=50°(right panel). Error bars represent the standard deviation.

Adjacency perturbations show a slight sensitivity to the water type at the sole blue wavelengths (see Bulgarelli and Zibordi, 2018a for details).

Biases induced by AE on the retrieved water-leaving radiance were theoretically estimated for two different atmospheric correction procedures (Bulgarelli et al., 2017; Bulgarelli and Zibordi, 2018a): those not deriving (AC-1) and those alternatively deriving (AC-2) the atmospheric properties from the remote sensing data itself. For AC-1 schemes biases increase with the land albedo (Bulgarelli and Zibordi, 2018a) (see Fig. 9). For AC-2 schemes, AE at those center-wavelengths from which atmospheric properties are inferred add significant perturbations at shorter wavelengths. Fig. 10 shows biases on tL_w (i.e., the water leaving radiance at the sensor, with t representing the atmospheric transmittance) theoretically estimated for a correction scheme determining the atmospheric properties from the NIR region through a power-law spectral extrapolation. Results indicate that AE at NIR wavelengths (affecting the retrieval of the atmospheric radiance) might compensate adjacency perturbations at the visible wavelengths. Consequently, biases on the retrieved water-leaving radiance are not directly correlated to the strength of the land spectral albedo. As an example, the impact of AE on the water

signal retrieved at the blue wavelengths might be larger for a vegetation land cover than for more highly reflective concrete or white sand. Compensations might even occur in the presence of snow. Results from Fig. 10 further indicate that percentage over- and underestimates of the radiance from Case-2 moderately sediment-dominated waters (e.g., northern Adriatic waters) at the coast might well exceed 100% at 443 nm in the presence of snow and green vegetation, respectively. It is mentioned that misestimates might increase about 4 times for CDOM-dominated waters, like those of the Baltic Sea (Bulgarelli and Zibordi, 2018a).

It is remarked that the retrieval of the atmospheric properties from MSI data is generally performed utilizing one or two short-wave infrared (SWIR) bands (e.g., those centered around 1600 and 2200 nm) (Vanhellemont and Ruddick, 2015). Although the analysis of AE at SWIR wavelengths (where land albedos generally consistently differ from values in the NIR) was not specifically addressed, it is nonetheless expected that analogous mechanisms of propagation of adjacency perturbations from the SWIR to the visible, as well as potential compensations between adjacency perturbations at SWIR and visible wavelengths, can occur.

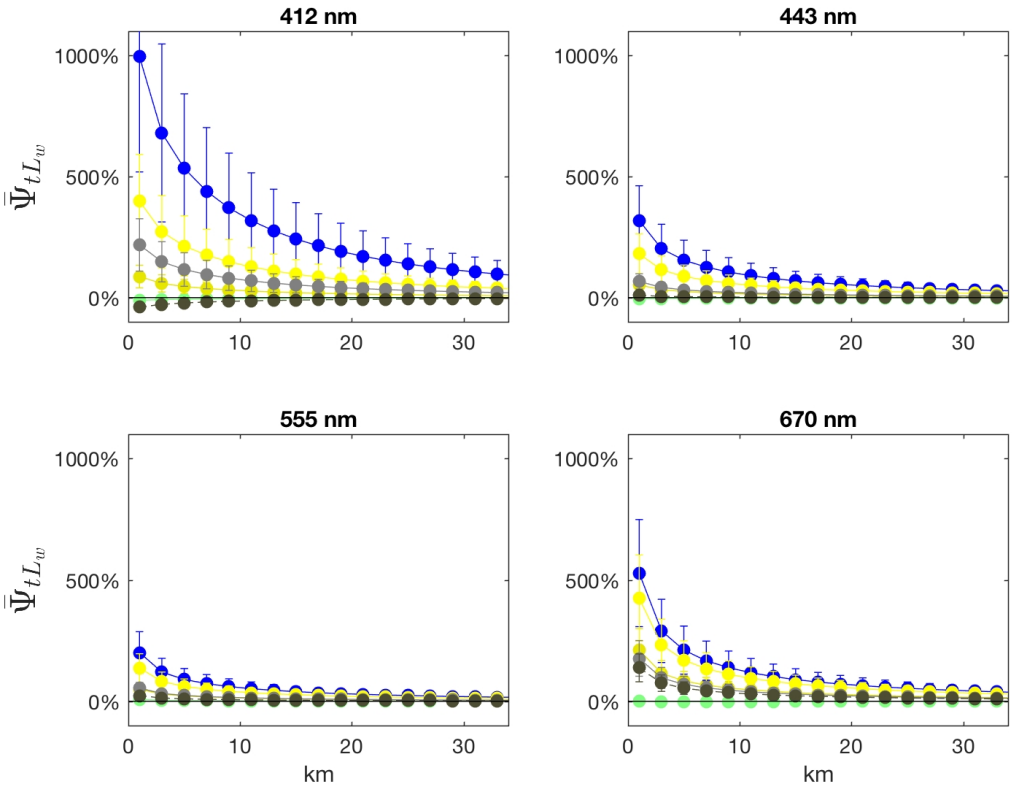

Figure 9. Values of average biases Ψ_{tLw} induced by adjacency perturbations on tL_w when derived with an AC-1 scheme. Results are given for NADR waters and representative land covers (see legend of Fig. 5) along the study transect as a function of the distance from the coast and at representative center-wavelengths. Error bars indicate ± 1 standard deviation (N = 24 test cases).

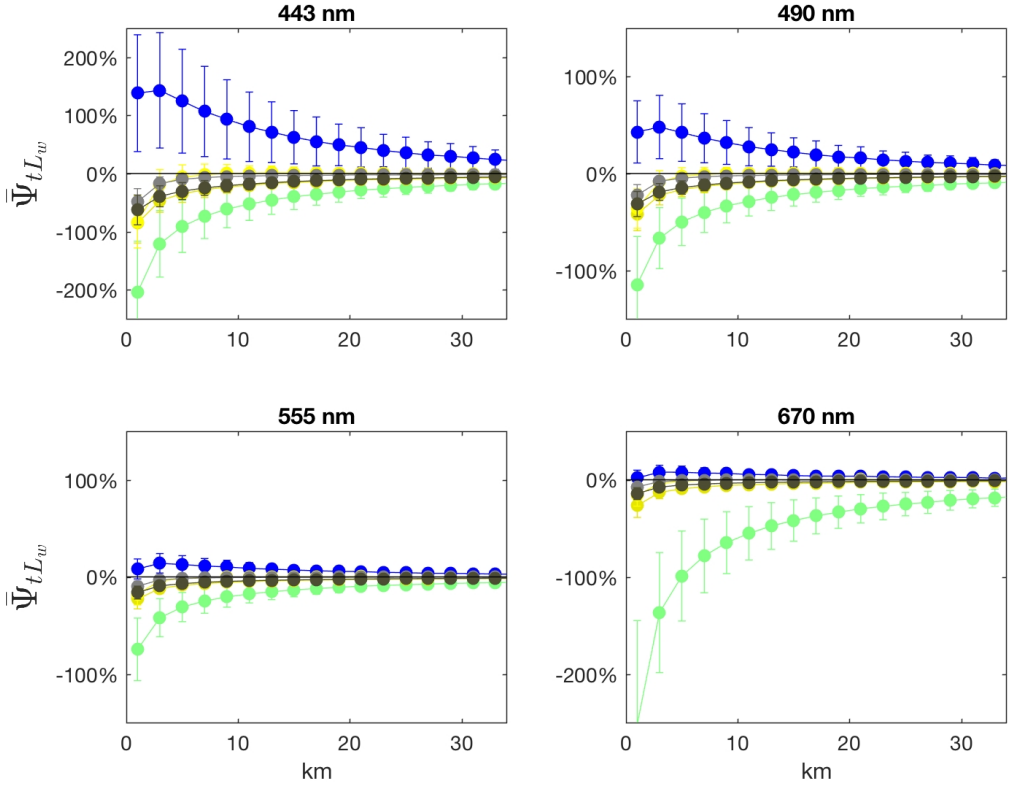

Figure 10. As in Figure 9, but for an AC-2 scheme applying a power law extrapolation to derive the aerosol properties from NIR center-wavelengths.

4.2 Seasonal results at the AAOT validation site

The AAOT measurement site is located in the northern Adriatic Sea (45.31 °N, 12.51 °E) at approximately 8 nautical miles southeast of the Venice Lagoon. The average water depth at the site is 17 m, and the composition of the sea floor is primarily sand and silt. The study area is mostly characterized by *i)* Case-2 waters moderately dominated by detritus or mineral particles from rivers discharge or tidal resuspension, *ii)* nearby land covered by a cropland ecosystem, and *iii)* continental aerosol from the nearby Po Valley. The site also exhibits purely maritime aerosol and Case-1 seawater features. These characteristics represent most of the properties of the northern Adriatic Sea region.

The comprehensive multi-annual record of *in situ* measurements performed at the AAOT (Zibordi et al., 2002 and 2009b; Berthon et al., 2002 and 2008b) allows a comprehensive characterization of the optical properties of atmosphere and water, enabling the definition of realistic and seasonally dependent test cases for the analysis of the AE.

Simulated adjacency perturbations at the AAOT have been determined at the SeaWiFS center-wavelengths (λ=412, 443, 490, 510, 555, 670, 765 and 865 nm) accounting for:

- *The actual coastal morphology, as extracted from the operational land/sea mask used in the REMBRANDT code (Bulgarelli and Mélin, 2000) to process SeaWiFS data from the northern Mediterranean Sea (Fig.11).*

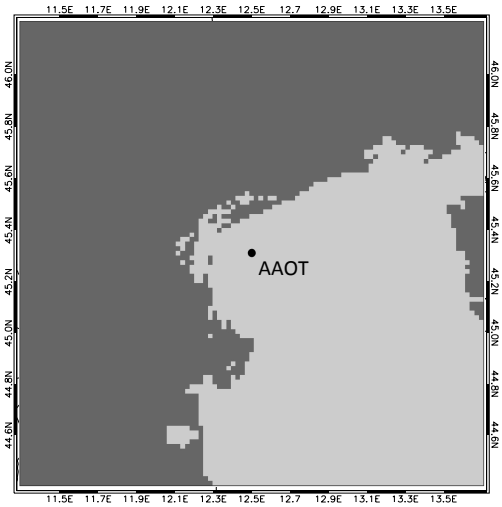

Figure 11. Land/sea mask utilized in the NAUSICAA MC simulations: land elements are indicated in dark grey, while sea elements in light grey. Each of the 100x100 square elements is ~1 km wide. The black circle represents the AAOT (45.31° N, 12.51° E).

- *The seasonal variation of the illumination conditions, identified by θ_0=25°, 45°, and 65°, for summer, mid-seasons and winter, respectively;*

- *Typical OLCI and MSI observation geometries at the AAOT (see Table 3);*

- *Average and extreme atmospheric conditions encountered in the region, identified by Ångström exponent v=1.4, 1.7 and 1.9, Ångström coefficient α=0.02, 0.05, 0.08, wind speed w=1, 3.3 and 6 ms^{-1}. Notably, the selected optical aerosol properties correspond to those mostly encountered at different AERONET-OC sites (Mélin et al., 2013).*

- *Average annual and intra-annual normalized remote sensing reflectances R_{rs} as measured in situ (Fig. 12). Negligible R_{rs} at NIR have been assumed, as justified by evidence of negligible differences in the simulation of L_{adj} at the AAOT when assuming a non-null NIR water signal (Bulgarelli et al., 2017).*

- *Annual and intra-annual land spectral albedos as inferred from a MODIS climatological database of reflectance products (Moody et al., 2008). Values, provided at MODIS land bands (λ= 470, 555, 659, 858 nm), have been interpolated at SeaWiFS center-wavelengths assuming a cropland ecosystem (Bulgarelli et al., 2014). Intra-annual spectral values of ρ_l are illustrated in Fig. 13.*

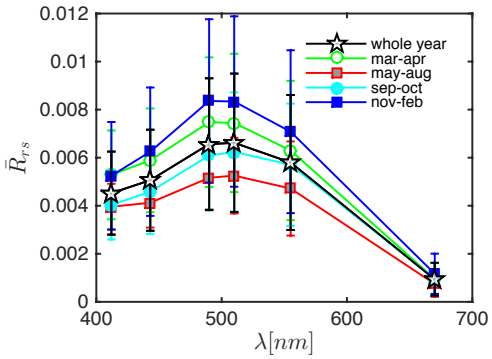

Figure 12. Spectral average values of in situ R_{rs} [sr^{-1}] adopted in the simulation of AE at the AAOT site: symbols represent different annual and intra-annual periods. Error bars indicate the standard deviation.

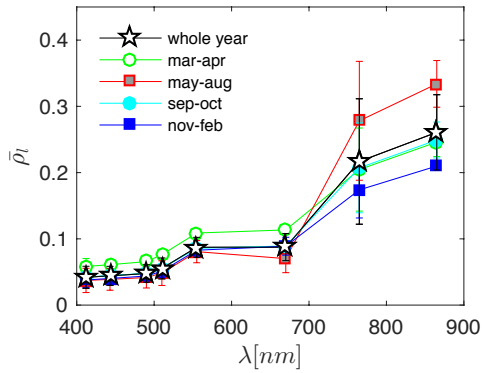

Figure 13. Spectral average values of ρ_l adopted in the simulation of AE at the AAOT site: symbols represent different annual and intra-annual periods. Error bars indicate the standard deviation.

Annual average values of $\bar{\xi}_{L_{tot}}$ at the AAOT for OLCI-RR, OLCI-FR and MSI are illustrated in Fig. 14 together with the radiometric sensitivity of the sensors. Average values are within ±0.5% at the visible center-wavelengths (negative up to 510 nm, and positive afterwards), while they rise up to ~2% at NIR center-wavelengths (see Bulgarelli et al., 2014 for a detailed discussion). Values are slightly smaller for MSI, due to its quasi-nadir geometry of observation. For MSI acquisitions, average perturbations appear to exceed NL at the sole 443 and 740 nm center-wavelengths. It is nevertheless recalled that values of NL for MSI might be underestimated, while AE at 740 nm might be slightly overestimated. Indeed, simulations of $\bar{\xi}_{L_{tot}}$ have been performed at the SeaWiFS center-wavelength 765 nm, where the land albedo might be sensibly larger since vegetation shows a steep spectral gradient around 700 nm (the so called *red edge*). AE in OLCI data are significantly above NL at NIR wavelengths. At visible wavelengths AE are larger than NL in RR acquisitions, but they are much close to noise in FR acquisitions. It is nevertheless noted that confidence on results at the blue wavelengths, where land and sea albedos are very similar, is lower (Bulgarelli et al., 2014).

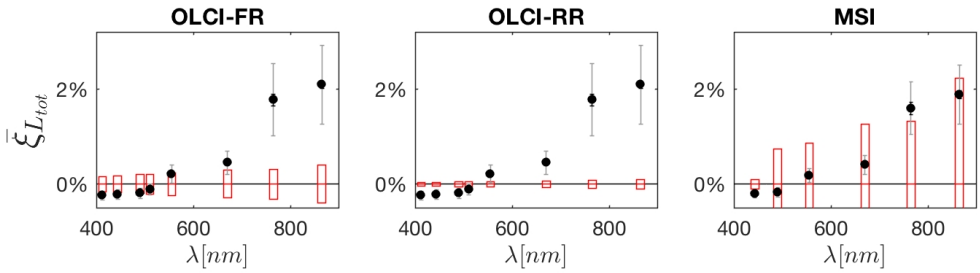

Figure 14. Spectral annual average values $\bar{\xi}_{L_{tot}}$ in correspondence of the AAOT at SeaWiFS equivalent center-wavelengths for each considered sensor. Black error bars represent the standard deviation; gray error bars the sample variance. Red block bars indicate NL from sensor specifications adjusted to L_{typ} (see Table 1 and 2).

The detectability of AE at the AAOT (i.e., when $\xi_{L_{tot}} > NL$) has a significant intra-annual variation (Bulgarelli and Zibordi, 2018b) (see Fig. 15). For both OLCI and MSI sensors, summer AE are below or close to NL up to 555 nm (at all visible wavelengths for MSI), but well above NL at NIR wavelengths, where they reach their yearly highest values. Winter AE are much lower at all wavelengths (due to dormant vegetation and low sun elevation): for MSI sole AE at 443 nm exceed NL, while for OLCI-FR AE are overall very close to noise.

For AC-1 schemes, average biases at the AAOT were estimated to be within ±5%. For the specific case of an AC-2 correction scheme determining the atmospheric properties from the NIR region and by adopting a power-law spectral extrapolation of adjacency perturbations on the derived atmospheric radiance, average biases at the AAOT were estimated being up to ~ −15% at 412, 443, and 670 nm.

Notably, the seasonal trend of simulated biases showed consistency with the intra-annual variation of biases observed in match-ups between *in situ* and satellite products derived with the NASA SeaDAS processing scheme from SeaWiFS and MODIS data (Zibordi et al., 2012a).

A validation exercise performed with SeaDAS on a sample of cloud-free SeaWiFS images acquired at the AAOT site, and alternatively ingesting original SeaWiFS data and SeaWiFS top-of-atmosphere data corrected for estimated adjacency contributions, indicated a significant decrease of annual and intra-annual biases at all wavelengths when correcting for AE (Bulgarelli et al., 2018c).

The same exercise additionally indicated AE at the AAOT larger than the estimated turbid water (TW) contributions in summer and mid-seasons, and hinted the occurrence of a systematic overestimate of the NIR water signal by the TW correction algorithm within the standard SeaDAS procedure, partially compensating for AE.

Notably, compensations of AE within the SeaDAS processing scheme allows explaining why previous analysis at sample validation sites did not provide firm evidence of appreciable AE in satellite primary products (Zibordi et al., 2009a).

The validation exercise allowed explaining the intra-annual variation in biases observed in SeaWiFS primary products acquired at the AAOT in the period 2002-2010 (Zibordi et al., 2012b) as the likely consequence of residual AE in data acquired in summer, and of misinterpretation of NIR atmospheric signal as TW contributions in data acquired in winter.

Results at the AAOT are considered representative of coastal environments characterized by mid-latitude atmospheric conditions and a cropland ecosystem, in the absence of snow.

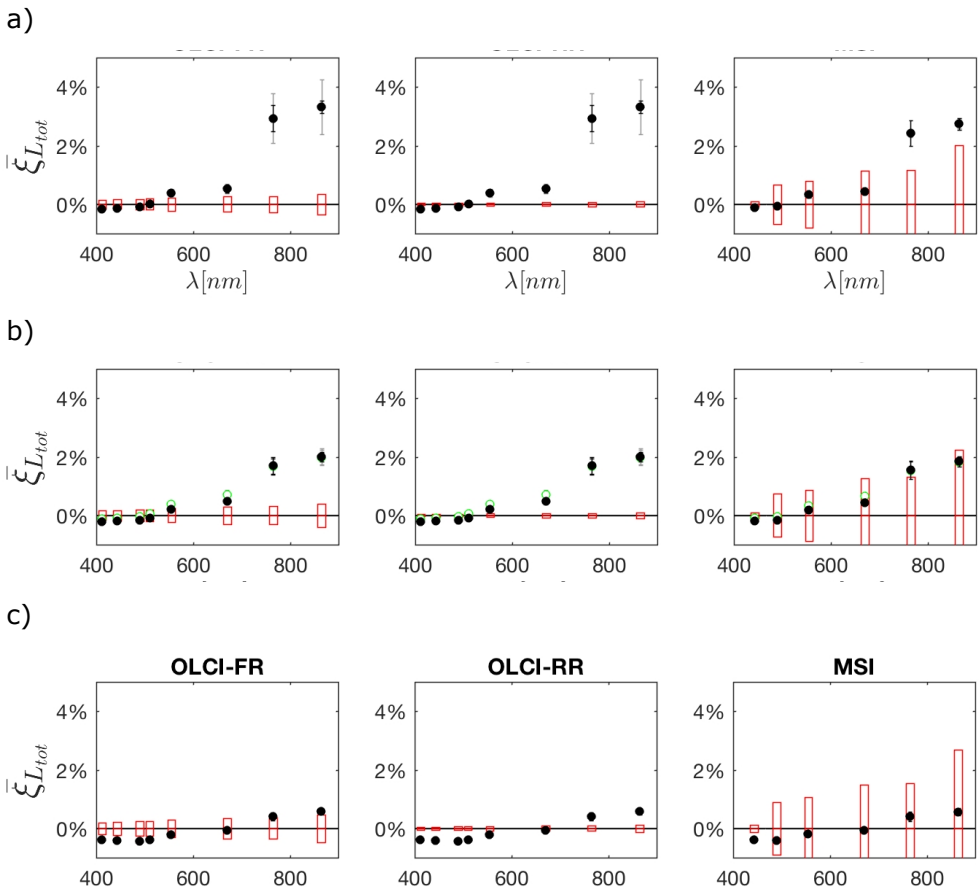

Figure 15. Spectral annual average values $\bar{\xi}_{L_{tot}}$ in correspondence of the AAOT at SeaWiFS equivalent center-wavelengths for each considered sensor and for a) summer, b) spring and autumn and c) winter acquisitions. Black error bars represent the standard deviation; gray error bars the sample variance. Red block bars indicate NL from sensor specifications adjusted to L_{typ} (see Table 1 and 2).

4.3 The adjacency field around the Lampedusa Island

The Lampedusa Island (35.52°, 12.57°), located in the southern Mediterranean Sea, hosts a station for climate observations managed by the Italian National Agency for New Technologies, Energy and Sustainable Economic Development (ENEA). This includes two sections: a ground-based laboratory (35.52°N, 12.63°E), operational since 1997 and dedicated to the investigation of changes in atmospheric composition and structure, and their effects on the surface radiation; and an oceanic buoy (35.49°, 12.47°) located at about 3.3 nautical miles southwest of the Island and dedicated since 2015 to investigate air-sea interactions and for the validation of OC satellite data products.

Oligotrophic waters surround the Lampedusa Island. Southern coastal waters, belonging to a marine reservoir that hinders the use of motorboats, are quite shallow (the depth at the oceanographic buoy is ~74 m). Northern waters are deeper, reaching around 300m depth at ~10 nautical miles from the coast.

Continental and anthropogenic particles originating from Europe, desert dust from Africa, as well as marine aerosols from the North Atlantic and the Mediterranean itself, are commonly present in the region (Meloni et al., 2006; Pace et al., 2005). Pure marine conditions only occur when the influence from the European and

African continents is very limited, and thus are rarely observed. Mixed conditions occur in the majority of the cases.

Evergreen spaced shrubs cover the semi-arid island.

The adjacency field surrounding the Lampedusa Island and its impact on OLCI acquisitions has been simulated at representative center-wavelengths (λ=490, 555, 670 and 865 nm) accounting for:

- *The actual coastal morphology, as extracted from the UMD Global 250 meter Land Water Mask (MOD44W MODIS product) (Carroll et al., 2009) (see Fig. 16).*

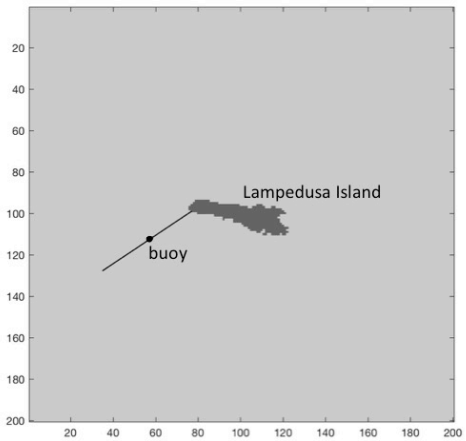

Figure 16. Land/sea mask utilized in NAUSICAA MC simulations around the Lampedusa Island: land elements are indicated in dark grey, sea elements in light grey. Each of the 200x200 square elements is ~232 m wide. The black circle represents the ENEA oceanographic buoy (35.49°, 12.47°).

- *The seasonal variation of the illumination conditions for a 10AM satellite pass (see Table 4);*

Table 4. Illumination and atmospheric conditions adopted in the simulations at the Lampedusa site.

Parameters	***average***	***January***	***August***
θ_0	48°	65°	35°
a	0.88	1.11	0.85
v	0.11	0.13	0.06
ω_0	0.8		
g	0.7		

- *Typical OLCI observation geometries (see Table 3);*

- *The seasonal variation of the atmospheric properties as extrapolated from observations acquired at the Lampedusa AERONET site (Meloni et al., 2006) in the period 2004-2017 (see Table 4, where g is the asymmetry parameter of the Single Term Henyey-Greenstein phase function adopted for the aerosol)*

- *Typical annual and intra-annual values of R_{rs} as extracted from a SeaWiFS multi-year climatological database of radiometric products (Fig. 17). R_{rs} has been assumed negligible at NIR, as justified by the presence of oligotrophic waters and by the above mentioned evidence of negligible differences in the simulation of L_{adj} when assuming a non-null NIR water signal (Bulgarelli et al., 2017).*

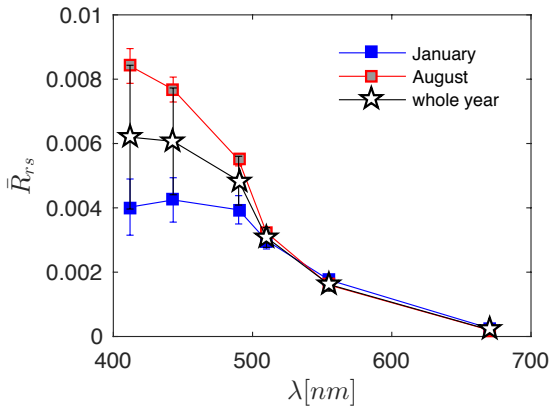

Figure 17. Average annual and intra-annual climatological spectral values of R_{rs} [sr^{-1}] adopted in the simulations. Error bars indicate the standard deviation.

- *Annual and intra-annual land spectral albedos as inferred from a MODIS climatological database of reflectance products (Moody et al., 2008) (see Fig. 18).*

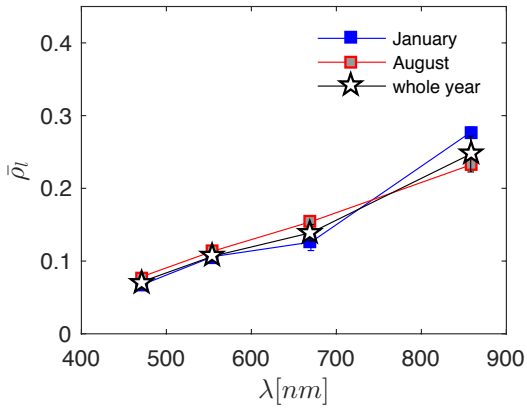

Figure 18. Average annual and intra-annual spectral values of climatological ρ_l adopted in the simulations. Error bars (not visible) indicate the standard deviation.

Annual average values of $\xi_{L_{tot}}$ in OLCI data over the marine region surrounding the Lampedusa Island are illustrated in Fig. 19 for λ=865 nm, where AE are spectrally the highest. Results are for θ_v=20°, ϕ_v=100°, θ_0=48° and ϕ_0=160°. Average land and water optical conditions are considered. Remarkably, the adjacency field shows a significantly different pattern south and north of the island. South of the island AE are always positive (up to

37%); north of the island a remarkable influence of the masked sea surface (term *W* of Eq. (1)) leads to negative AE (up to -1%) in correspondence of the reflected sunbeam. Notably, the area affected by significant negative adjacency contributions becomes larger at shorter wavelengths (not shown here), due to the lower values of land albedo. Masked sea surface contributions highly depend on the surface reflectance anisotropy, i.e., on wind speed and direction, and on the sun position. This hinders the possibility to give a general evaluation of the impact of AE in the northern marine region. In the remaining water region, adjacency contributions at 865 nm exceed NL up to ~5-7 km offshore for OLCI-FR, and up to 10-12 km offshore for OLCI-RR.

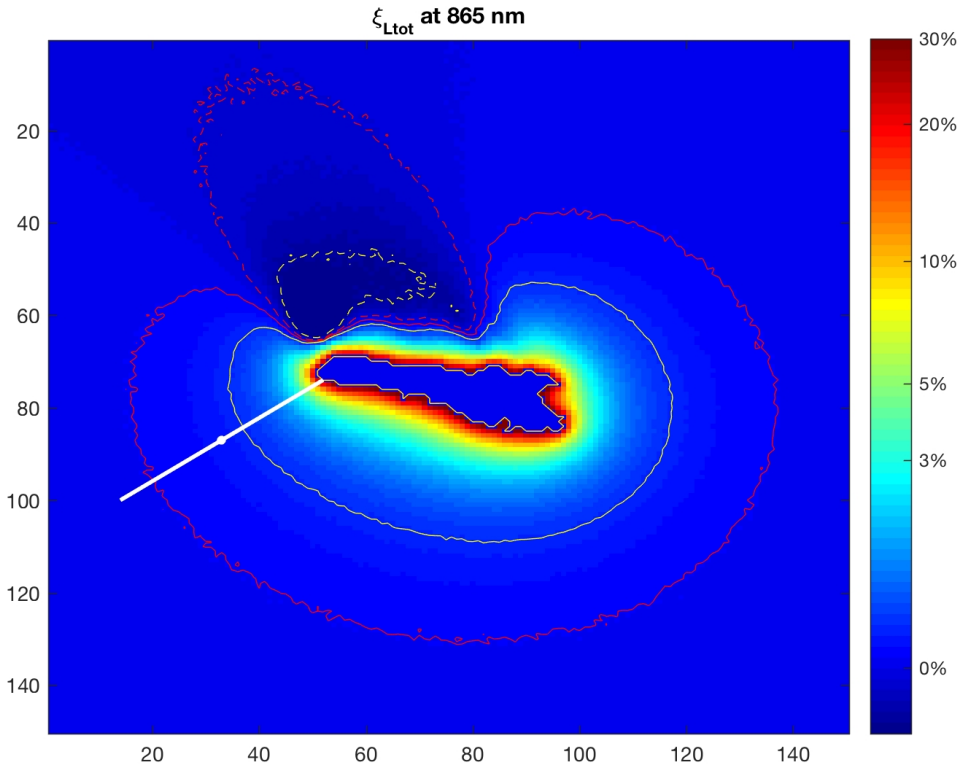

Figure 19. ξ_{Ltot} at 865 nm for θ_v=20°, ϕ_v=100° and average illumination, land and water optical conditions. The white straight line indicates the transect intercepting the oceanographic buoy (white dot) and extending up to 13 km offshore. The yellow and red contour lines designate NL for OLCI-FR and OLCI-RR, respectively. Dashed contour lines are for –NL, full contour lines for +NL.

Results along the transect depicted in Fig. 19, and assumed as representative of the marine region south of the island, are further analyzed accounting for the whole set of observation conditions listed in Table 3 and 4. Mean adjacency contributions at representative center-wavelengths are illustrated in Fig. 20 together with the standard deviation σ. It is recalled that adjacency perturbations larger than the average occur for slanted observations and in summer. Adjacency perturbations lower than the average occur in winter.

Results from Fig. 20 indicate that AE becomes lower than NL in all observation conditions and at all center-wavelengths with a 99.7% level of confidence (corresponding to 3σ) at ~8 and 14 km along the transect for OLCI-FR and OLCI-RR, respectively.

By also considering that system vicarious calibrations (SVC) rely on the application of a number of images, which may lead to a decrease of NL, still a fully confident avoidance of AE in the vicarious calibration of OLCI data might suggest to locate the site even further away from the coast.

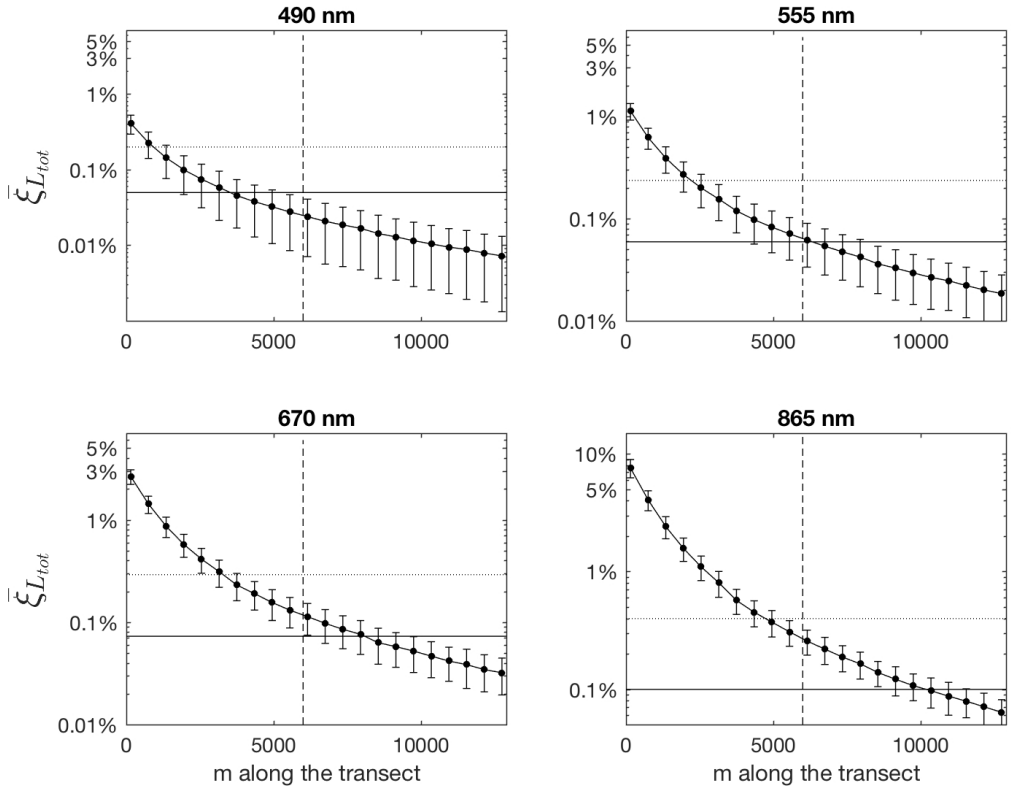

Figure 20. Mean values of ξ_{Ltot} at representative center-wavelengths along the transect depicted in Fig. 16. The vertical dashed line indicates the position of the oceanographic buoy. The horizontal dotted line indicates NL for OLCI_FR, while the horizontal full line NL for OLCI-RR. Grey error bars indicate ±1σ.

5. Conclusions

The generation of satellite OC data products meeting the GCOS requirements for the construction of CDRs, implies the minimization of uncertainties affecting the calibration of the satellite sensor and the atmospheric correction process. This strictly applies to the delivery by the Copernicus Programme of satellite OC data from the Sentinel-2 and Sentinel-3 missions.

Among uncertainties affecting OC products, this work focused on those perturbations induced by the radiance reflected by the nearby land and diffused by the atmosphere into the field-of-view of the OC sensor: the so called *adjacency effects*.

By relying on studies led by the JRC, this work has summarized results from the theoretical evaluations of AE in marine observations from OLCI and MSI sensors, and their impact on radiometric primary products.

Results showed AE that still exceed the radiometric noise thresholds up to ~36 km (20 km for MSI) from a continental coast of highly reflecting land covers (like white sand, snow, dry vegetation, concrete). In the presence of green vegetation or bare soil, AE drop below NL at a shorter distance from the coast, but such a distance increases with the sensor radiometric sensitivity. Indeed, AE are lower than NL at a distance shorter than 36 km at the sole red wavelengths with green vegetation in OLCI-RR measurements. Since cropland is a composite of green vegetation and bare soil (close to the former in summer, and to the latter in winter), similar considerations apply.

Results additionally showed a significant increase of AE with the sensor viewing angle, and with the sun elevation. AE showed further dependence on the sun and satellite position with respect to land. The former dependence is more evident when the land albedo is low, the second for highly reflecting land covers.

As expected, results indicated lower AE in the surrounding of the small Lampedusa Island. Here simulations highlighted that satellite data of the marine region lying in the anti-solar half-plane (i.e., north of the island) are largely affected by contributions from the masked sea surface (the so called Fresnel mask), leading to negative adjacency contributions. South of the island AE are instead always positive, with mean AE larger than NL up to ~7 and 12 km offshore for OLCI-FR and OLCI-RR, respectively. By accounting for a further reduction of NL when combining several OLCI images (e.g., 100) for calibration purpose, OLCI-RR data are expected to be free from adjacency perturbations in all observational cases from ~50 km offshore with a ~99.7% level of confidence.

Biases induced by AE on derived radiometric products highly depend on the atmospheric correction procedure applied. For a procedure estimating the atmospheric properties from the NIR wavelengths with a power law spectral extrapolation, biases induced by AE at visible and NIR wavelengths might compensate each other. As a consequence of this, biases do not display proportionality to the strength of the land albedo. For example, the impact of AE on the water signal retrieved at the blue wavelengths might be larger for a vegetation land cover than for more highly reflective concrete or white sand. Compensations might even occur in the presence of snow. Notably, percentage over- and underestimates of the radiance from Case-2 moderately sediment-dominated waters (e.g., northern Adriatic waters) at the coast might well exceed 100% at 443 nm in the presence of snow and green vegetation, respectively. Misestimates might increase about 4 times

for CDOM-dominated waters, like those of the Baltic Sea (Bulgarelli and Zibordi, 2018a).

In the presence of vegetation (the most diffuse coastal ecosystem in Europe) biases are expected to induce significant negative biases on the water leaving radiance at the blue and red wavelengths.

Based on results from (Bulgarelli et al., 2014; 2017; 2018c; Bulgarelli and Zibordi, 2018a; 2018b), the following general considerations can be drawn:

- *Results point out a **clear and urgent need to account for AE** in the processing of OC data from coastal areas. AE are estimated to exceed turbid water contributions at the AAOT, and are shown to exceed the radiometric noise thresholds of OLCI and MSI in the majority of cases up to several tens of km from the coast.*
    - *For MSI and OLCI-FR measurements, the detectability of AE at large distance from the coast might occur in the sole presence of highly reflecting land covers (such as snow, white sand, dry vegetation and concrete). Green vegetation and bare soil might lead to AE lower than the noise thresholds at shorter distances from the coast.*
    - *Conversely, AE from all land covers (i.e., green vegetation and bare soil included) exceed NL in OLCI-RR measurements (a part from green vegetation at the red wavelengths).*

- *The theoretical analysis on dependences of AE highlights that an algorithm for the modeling and correction of AE should account for:*
    - *sensor viewing angle (AE consistently increase with θ, nearly doubling when θ increases from 20^o to 50^o)*
    - *illumination conditions (AE significantly decrease with θ_0)*
    - *atmospheric conditions. There is evidence that at some distance from the coast the phenomenon is Rayleigh-dominated (to be analyzed in future investigations).*
    - *When sea and land albedos are very similar (as for green vegetation, bare soil and cropland at the blue wavelengths) the following aspects become relevant:*
        - *the anisotropy of surface reflectance*
        - *the optical properties of the water*
        - *the position of the sun with respect to land.*
    - *When the land albedo is significantly larger than the sea one (as for all land covers at NIR, and for snow, white sand, dry vegetation and concrete at all wavelengths):*
        - *the optical properties of the water and its surface are not crucial in the determination of the AE,*
        - *but the position of the sensor with respect of the land becomes relevant.*

- *Results additionally point out that **the land albedo should be measured at the same time and at the same wavelengths of OC measurements**. This is particularly important at those NIR/SWIR bands used to derive the atmospheric properties, especially when band ratios are involved and when those bands are located in a region of steep spectral gradient of the land albedo (as for the vegetation red edge).*

- *Results point out that, for a retrieval scheme deriving the aerosol properties from NIR/SWIR bands,* ***biases on radiometric primary products*** *are not directly dependent on the strength of the land albedo at the analyzed wavelengths, because compensations might occur between AE at the visible and NIR wavelengths*

  As well, AE might be compensated by misestimates of other radiance contributions within the atmospheric correction code (e.g., overestimates of TW contributions at NIR wavelengths)

- *It is additionally remarked that AE should be considered when selecting the* ***location of a site for the vicarious calibration of Copernicus products****: the site should be put at a safe distance from the coast to avoid AE, or alternatively the utilized atmospheric correction code should account for AE. For the specific case of the Lampedusa Island, it is foreseen that vicarious calibrations of OLCI data acquired in the southern marine region are affected by appreciable AE up to about 15 km from the coast. By additionally considering that system vicarious calibrations rely on the application of a number of images, which may lead to a decrease of NL, still a fully confident avoidance of AE in the vicarious calibration of OLCI data might suggest to locate the site even further away from the coast.*

References

Adler-Golden, S. M., Matthew, M. W., Bernstein, L. S., Levine, R. Y., Berk, A., Richtsmeier, S. C., et al. (1999). Atmospheric correction for short-wave spectral imagery based on MODTRAN4. In M. R. Descour and S. S. Shen (Eds.), (Vol. 3753, pp. 61–69). Presented at the Proceedings of SPIE - The International Society for Optical Engineering, SPIE. http://doi.org/10.1117/12.366315

Antoine, D., and Morel, A. (1999). A multiple scattering algorithm for atmospheric correction of remotely sensed ocean colour (MERIS instrument): Principle and implementation for atmospheres carrying various aerosols including absorbing ones. *International Journal of Remote Sensing*, *20*(9), 1875–1916. http://doi.org/10.1080/014311699212533

Baldridge, A. M., Hook, S. J., Grove, C. I., and Rivera, G. (2009). The ASTER spectral library version 2.0. *Remote Sensing of Environment*, *113*(4), 711–715. http://doi.org/10.1016/j.rse.2008.11.007

Berthon, J. F., Zibordi, G., Doyle, J. P., Grossi, S., van der Linde, D., and Targa, C. (2002). Coastal Atmosphere and Sea Time Series (CoASTS), Part 2: Date analysis. *NASA Technical Memorandum - SeaWIFS Postlaunch Technical Report Series*, (20), 1–25.

Berthon, J., Mélin, F., and Zibordi, G. (2008a). Ocean colour remote sensing of the optically complex European seas. *Remote Sensing of the European Seas*, 35–52.

Berthon, J.-F., and Zibordi, G. (2010). Optically black waters in the northern Baltic Sea. *Geophysical Research Letters*, *37*(9), L09605. http://doi.org/10.1029/2010GL043227

Berthon, J.-F., Mélin, F., and Zibordi, G. (2008b). Ocean colour remote sensing of the optically complex European Seas. In V. Barale and M. Gade (Eds.), *Remote Sensing of the European Seas* (pp. 35–52). Dordrecht: Springer Netherlands. http://doi.org/10.1007/978-1-4020-6772-3_3

Bélanger, S., Ehn, J. K., and Babin, M. (2007). Impact of sea ice on the retrieval of water-leaving reflectance, chlorophyll a concentration and inherent optical properties from satellite ocean color data. *Remote Sensing of Environment*, *111*(1), 51–68.

Bulgarelli, B., and Zibordi, G. (2003). Remote sensing of ocean colour: Accuracy assessment of an approximate atmospheric correction method. *International Journal of Remote Sensing*, *24*(3), 491–509. http://doi.org/10.1080/01431160304985

Bulgarelli, B., and Zibordi, G. (2018a). On the detectability of adjacency effects in ocean color remote sensing of mid-latitude coastal environments by SeaWiFS, MODIS-A, MERIS, OLCI, OLI and MSI. *Remote Sensing of Environment*, *209*, 423–438. http://doi.org/10.1016/j.rse.2017.12.021

Bulgarelli, B., and Zibordi, G. (2018b). Seasonal Impact of Adjacency Effects on Ocean Color Radiometry at the AAOT Validation Site. *Geoscience and Remote Sensing Letters, IEEE*, *15*(4), 488–492. http://doi.org/10.1109/LGRS.2017.2781900

Bulgarelli, B., Giuseppe, Z., and Melin, F. (2018c). On the minimization of adjacency effects in SeaWiFS primary data products from coastal areas. *Optics Express*, 26(18), A709-A728, http://doi.org/10.1364/OE.26.00A709

Bulgarelli, B., Kiselev, V., and Zibordi, G. (2014). Simulation and analysis of adjacency effects in coastal waters: a case study, *53*(8), 1523. http://doi.org/10.1364/AO.53.001523

Bulgarelli, B., Kiselev, V., and Zibordi, G. (2017). Adjacency effects in

satellite radiometric products from coastal waters: a theoretical analysis for the northern Adriatic Sea. *Applied Optics*, *56*(4), 854–16. http://doi.org/10.1364/AO.56.000854

Bulgarelli, B., Kisselev, V., and Roberti, L. (1999). Radiative transfer in the atmosphere-ocean system: the finite-element method, *38*(9), 1530–1542.

Carroll, M. L., Townshend, J. R., DiMiceli, C. M., Noojipady, P., and Sohlberg, R. A. (2009). A new global raster water mask at 250 m resolution. *International Journal of Digital Earth*, *2*(4), 291–308. http://doi.org/10.1080/17538940902951401

Gordon, H. W., and Wang, M. (1994). Retrieval of water-leaving radiance and aerosol optical thickness over the oceans with SeaWiFS: a preliminary algorithm, *33*(3), 443–452. http://doi.org/10.1364/AO.33.000443

Heege, T., Kiselev, V., Wettle, M., and Hung, N. N. (2014). Operational multi-sensor monitoring of turbidity for the entire Mekong Delta. *International Journal of Remote Sensing*, *35*(8), 2910–2926. http://doi.org/10.1080/01431161.2014.890300

Houborg, R., and McCabe, M. F. (2017). Impacts of dust aerosol and adjacency effects on the accuracy of Landsat 8 and RapidEye surface reflectances. *Remote Sensing of Environment*, *194*, 127–145. http://doi.org/10.1016/j.rse.2017.03.013

Hu, C., Feng, L., Lee, Z., Davis, C. O., Mannino, A., McClain, C. R., and Franz, B. A. (2012). Dynamic range and sensitivity requirements of satellite ocean color sensors: learning from the past, *51*(25), 6045–6062.

IGBP Land Ecosystem Classification Map Image. (2013). IGBP Land Ecosystem Classification Map Image. Retrieved April 21, 2013, from http://modis-atmos.gsfc.nasa.gov/ECOSYSTEM/

Kaufman, Y. J. (1979). Effect of the Earth's atmosphere on contrast for zenith observation. *J. Geophys. Res*, *84*(C6), 3165–3172.

Kaufman, Y. J. (1984). Atmospheric effect on spatial resolution of surface imagery, *23*(19), 3400–3408. http://doi.org/10.1364/AO.23.003400

Kiselev, V., Bulgarelli, B., and Heege, T. (2015). Sensor independent adjacency correction algorithm for coastal and inland water systems. *Remote Sensing of Environment*, *157*, 85–95. http://doi.org/10.1016/j.rse.2014.07.025

Kisselev, V., and Bulgarelli, B. (2004). Reflection of light from a rough water surface in numerical methods for solving the radiative transfer equation. *Journal of Quantitative Spectroscopy and Radiative Transfer*, *85*(3-4), 419–435.

Malenovský, Z., Rott, H., Cihlar, J., Schaepman, M. E., García-Santos, G., Fernandes, R., and Berger, M. (2012). Sentinels for science: Potential of Sentinel-1, -2, and -3 missions for scientific observations of ocean, cryosphere, and land. *Remote Sensing of Environment*, *120*(C), 91–101. http://doi.org/10.1016/j.rse.2011.09.026

Martonchik, J. V., Bruegge, C. J., and Strahler, A. H. (2000). A review of reflectance nomenclature used in remote sensing. *Remote Sensing Reviews*, *19*(1-4), 9–20. http://doi.org/10.1080/02757250009532407

Masek, J. G., Vermote, E. F., Saleous, N. E., Wolfe, R., Hall, F. G., Huemmrich, K. F., et al. (2006). A Landsat Surface Reflectance Dataset for North America, 1990–2000. *Geoscience and Remote Sensing Letters, IEEE*, *3*(1), 68–72. http://doi.org/10.1109/LGRS.2005.857030

Meloni, D., di Sarra, A., Pace, G., and Monteleone, F. (2006). Aerosol optical properties at Lampedusa (Central Mediterranean). 2. Determination of single scattering albedo at two wavelengths for different aerosol types. *Atmospheric Chemistry and Physics*, *6*(3), 715–727.

http://doi.org/10.5194/acp-6-715-2006
Mélin, F., Sclep, G., Jackson, T., and Sathyendranath, S. (2016). Uncertainty estimates of remote sensing reflectance derived from comparison of ocean color satellite data sets. *Remote Sensing of Environment*, *177*, 107–124. http://doi.org/10.1016/j.rse.2016.02.014
Mélin, F., Zibordi, G., and Holben, B. N. (2013). Assessment of the Aerosol Products From the SeaWiFS and MODIS Ocean-Color Missions. *IEEE Geoscience and Remote Sensing Letters*, *10*(5), 1185–1189. http://doi.org/10.1109/LGRS.2012.2235408
Moody, E. G., King, M. D., Schaaf, C. B., and Platnick, S. (2008). MODIS-Derived Spatially Complete Surface Albedo Products: Spatial and Temporal Pixel Distribution and Zonal Averages. *Journal of Applied Meteorology and Climatology*, *47*(11), 2879–2894. http://doi.org/10.1175/2008JAMC1795.1
Moses, W. J., Bowles, J. H., Lucke, R. L., and Corson, M. R. (2012). Impact of signal-to-noise ratio in a hyperspectral sensor on the accuracy of biophysical parameter estimation in case II waters. *Optics Express*, *20*(4), 4309–4330. http://doi.org/10.1364/OE.20.004309
Otterman, J., and Fraser, R. S. (1979). Adjacency effects on imaging by surface reflection and atmospheric scattering: cross radiance to zenith, *18*(16), 2852–2860. http://doi.org/10.1364/AO.18.002852
Pace, G., di Sarra, A., Meloni, D., Piacentino, S., and Chamard, P. (2005). Aerosol optical properties at Lampedusa (Central Mediterranean) ? 1. Influence of transport and identification of different aerosol types. HAL - CCSD.
Pearce, W. A. (1986). Monte Carlo study of the atmospheric spread function, *25*(3), 438–447. http://doi.org/10.1364/AO.25.000438
Reinersman, P. N., and Carder, K. L. (1995). Monte Carlo simulation of the atmospheric point-spread function with an application to correction for the adjacency effect, *34*(21), 4453–4471. http://doi.org/10.1364/AO.34.004453
Richter, R., and Schlapfer, D. (2018). *Atmospheric / Topographic Correction for Satellite Imagery* (pp. 1–280).
Ruddick, K. G., Ovidio, F., and Rijkeboer, M. (2000). Atmospheric correction of SeaWiFS imagery for turbid coastal and inland waters, *39*(6), 897–912.
Santer, R., and Schmechtig, C. (2000). Adjacency effects on water surfaces: primary scattering approximation and sensitivity study, *39*(3), 361–375.
Santer, R., and Zagolski, F. (2009). *ICOL - Improve Contrast between Ocean and Land* (1st ed.). (F. Universite' de Littoral, Ed.)*brockmann-consult.de* (pp. 1–15).
Sei, A. (2007). Analysis of adjacency effects for two Lambertian half-spaces. *International Journal of Remote Sensing*, *28*(8), 1873–1890. http://doi.org/10.1080/01431160600851868
Sei, A. (2015). Efficient correction of adjacency effects for high-resolution imagery: integral equations, analytic continuation, and Padé approximants, *54*(12), 3748–11. http://doi.org/10.1364/AO.54.003748
Sterckx, S. (2017). iCOR plugin for SNAP toolbox, 1–20.
Sterckx, S., Knaeps, S., Kratzer, S., and Ruddick, K. (2015). SIMilarity Environment Correction (SIMEC) applied to MERIS data over inland and coastal waters. *Remote Sensing of Environment*, *157*, 96–110. http://doi.org/10.1016/j.rse.2014.06.017
Tanre, D., Herman, M., Deschamps, P. Y., and Leffe, A. de. (1979). Atmospheric Modeling For Space Measurements Of Ground Reflectances, Including Bidirectional Properties, *18*(21), 3587. http://doi.org/10.1364/AO.18.003587
vanhellemont, Q., and Ruddick, K. (2015). Advantages of high quality SWIR

bands for ocean colour processing: Examples from Landsat-8. *Remote Sensing of Environment*, *161*(C), 89–106. http://doi.org/10.1016/j.rse.2015.02.007

Vermote, E. F., and Vermeulen, A. (1999). *Atmospheric correction algorithm: spectral reflectances (MOD09)* (4 ed.). *ATBD version*. NASA.

Yang, H., Gordon, H. R., and Zhang, T. (1995). Island perturbation to the sky radiance over the ocean: simulations, *34*(36), 8354–8362.

Zibordi, G., Berthon, J. F., Doyle, J. P., Grossi, S., van der Linde, D., Targa, C., and Alberotanza, L. (2002). Coastal Atmosohere and Sea Time Series (CoASTS), Part 1: A tower-based, long-term measurement program. *NASA Technical Memorandum - SeaWIFS Postlaunch Technical Report Series*, (19), 1–29.

Zibordi, G., Berthon, J. F., Mélin, F., and D'Alimonte, D. (2011). Cross-site consistent in situ measurements for satellite ocean color applications: The BiOMaP radiometric dataset. *Remote Sensing of Environment*, *115*(8), 2104–2115. http://doi.org/10.1016/j.rse.2011.04.013

Zibordi, G., Berthon, J. F., Mélin, F., D'Alimonte, D., and Kaitala, S. (2009a). Validation of satellite ocean color primary products at optically complex coastal sites: Northern Adriatic Sea, Northern Baltic Proper and Gulf of Finland. *Remote Sensing of Environment*, *113*(12), 2574–2591.

Zibordi, G., Mélin, F., and Berthon, J. F. (2012a). Intra-annual variations of biases in remote sensing primary ocean color products at a coastal site. *Remote Sensing of Environment*, *124*, 627–636. http://doi.org/10.1016/j.rse.2012.06.016

Zibordi, G., Mélin, F., and Berthon, J. F. (2012b). Trends in the Bias of Primary Satellite Ocean-Color Products at a Coastal Site. *IEEE Geoscience and Remote Sensing Letters*, *9*(6), 1056–1060. http://doi.org/10.1109/LGRS.2012.2189753

Zibordi, G., Mélin, F., Berthon, J., Holben, B., Slutsker, I., Giles, D., et al. (2009b). AERONET-OC: A Network for the Validation of Ocean Color Primary Products. *Journal of Atmospheric and Oceanic Technology*, *26*(8), 1634–1651.

List of abbreviations and definitions

AAOT	Aqua Alta Oceanogrpahic Tower
AC	Atmospheric Correction
AE	Adjacency Effects
AERONET-OC	Ocean Color component of the Aerosol Robotic Network
ASTER	Advanced Spaceborne Thermal Emission and Reflection Radiometer
BioMap	Bio-Optical mapping of Marine Properties
BLK	Black Sea
BLTS	Baltic Sea
CDOM	Color Dissolved Organic Matter
CDR	Climate Data Record
CMEMS	The Copernicus Marine Environment Monitoring Service
ECHN	English Channel
ECV	Essential Climate Variable
EOV	Essential Ocean Variable
EMED	East Mediterranean Sea
ENEA	
EO	Earth Observation
EOSS	Earth Observation Support to Copernicus Climate and Marine Services
EU	European Union
DHR	Directional Hemispherical Reflectance
FEM	Finite Element Method
GCOS	Global Climate Observation System
GOOS	Global Ocean Observation System
FR	Full spatial Resolution
JRC	Joint Research Centre
LIGS	Ligurian Sea
MERIS	Medium Resolution Imaging Spectrometer
MC	MonteCarlo
MODIS	Moderate Resolution Imaging Spectroradiometer
MSI	MultiSpectral Imagery
NADR	northern Adriatic Sea
NASA	National Aeronautics and Space Administration
NAUSICAA	Novel Adjacency Perturbation Simulator for Coastal Areas
NIR	Near Infrared
NL	Noise Level
OLCI	Ocean and Land Colour Instrument
OLI	Operational Land Imager
RR	Reduced spatial Resolution
SeaDAS	SeaWiFS Data Analysis System
SeaWiFS	Sea Wide Field of View Sensor
SNR	Signal to Noise Ratio
SVC	System Vicarious Calibration
SWIR	Short-Wave Infrared
TOA	Top-of-Atmosphere
TW	Turbid Water
Chl_a	Chlorophyll-*a* concentration
ξ_{Ltot}	$100 \cdot L_{adj} / L_{tot}$
L_{adj}	Adjacency Radiance
L_{tot}	TOA radiance
L_{typ}	Typical TOA radiance for cloud-free ocean scenes
L_W	Water-leaving radiance

L_{WN}	Normalized water-leaving radiance
R_{RS}	Remote sensing reflectance
t	Atmospheric transmittance
w	wind speed
λ	wavelength
α	Ångström coefficient
v	Ångström exponent
ρ_l	Land Albedo
ρ_{sea}	Albedo of the Sea
τ_a	Aerosol optical thickness
σ	Standard deviation
θ_v	Sensor viewing angle
ϕ_v	Satellite Azimuth Angle
θ_0	Sun Zenith Angle
ϕ_0	Sun Azimuth Angle

List of figures

List of tables

GETTING IN TOUCH WITH THE EU

In person

All over the European Union there are hundreds of Europe Direct information centres. You can find the address of the centre nearest you at: https://europa.eu/european-union/contact_en

On the phone or by email

Europe Direct is a service that answers your questions about the European Union. You can contact this service:

- by freephone: 00 800 6 7 8 9 10 11 (certain operators may charge for these calls),

- at the following standard number: +32 22999696, or

- by electronic mail via: https://europa.eu/european-union/contact_en

FINDING INFORMATION ABOUT THE EU

Online

Information about the European Union in all the official languages of the EU is available on the Europa website at: https://europa.eu/european-union/index_en

EU publications
You can download or order free and priced EU publications from EU Bookshop at: https://publications.europa.eu/en/publications. Multiple copies of free publications may be obtained by contacting Europe Direct or your local information centre (see https://europa.eu/european-union/contact_en).

KJ-1A-29350-EN-N

The European Commission's science and knowledge service

Joint Research Centre

JRC Mission

As the science and knowledge service of the European Commission, the Joint Research Centre's mission is to support EU policies with independent evidence throughout the whole policy cycle.

EU Science Hub

ec.europa.eu/jrc

@EU_ScienceHub

EU Science Hub - Joint Research Centre

Joint Research Centre

EU Science Hub

Publications Office

doi:10.2760/178467

ISBN 978-92-79-96686-6